Joakim Halldin Stenlid, Mikaela Görlin, Oscar Diaz-Morales, Bernadette Davies, Vladimir Grigorev, David Degerman, Aleksandr Kalinko, Mia Börner, Mikhail Shipilin, Matthias Bauer, Alessandro Gallo, Frank Abild-Pedersen, Michal Bajdich, Anders Nilsson, and Sergey Koroidov\*



Downloaded via 139.63.203.201 on July 28, 2025 at 15:14:16 (UTC). See https://pubs.acs.org/sharingguidelines for options on how to legitimately share published articles

Cite This: J. Am. Chem. Soc. 2025, 147, 4120-4134



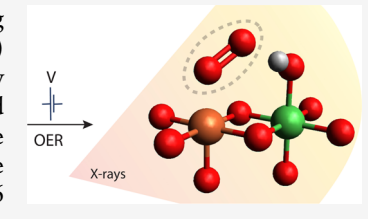
**ACCESS** 

Metrics & More

Article Recommendations

Supporting Information

**ABSTRACT:** Iron-doped nickel oxyhydroxides,  $Ni_x(Fe_{1-x})O_vH_z$ , are among the most promising oxygen evolution reaction (OER) electrocatalysts in alkaline environments. Although iron (Fe) significantly enhances the catalytic activity, there is still no clear consensus on whether Fe directly participates in the reaction or merely acts as a promoter. To elucidate the Fe's role, we performed operando X-ray spectroscopy studies supported by DFT on  $Ni_x(Fe_{1-x})O_yH_z$  electrocatalysts. We probed the reversible changes in the structure and electronic character of  $Ni_x(Fe_{1-x})O_yH_z$  as the electrode potential is cycled between the resting (here at 1.10  $V_{\rm RHE}$ ) and operational states (1.66  $V_{\rm RHF}$ ). DFT calculations and XAS simulations on a library of Fe structures in various NiO<sub>v</sub>H<sub>z</sub>



environments are in favor of a distorted local octahedral  $Fe(III)O_3(OH)_3$  configuration at the resting state with the  $NiO_vH_z$  scaffold going from  $\alpha$ -Ni(OH)<sub>2</sub> to  $\gamma$ -NiOOH as the potential is increased. Under catalytic conditions, EXAFS and HERFD spectra reveal changes in p-d mixing (covalency) relative to the resting state between O/OH ligands and Fe leading to a shift from octahedral to square pyramidal coordination at the Fe site. XES measurements and theoretical simulations further support that the Fe equilibrium structure remains in a formal Fe(III) state under both resting and operational conditions. These spectral changes are attributed to potential dependent structural rearrangements around Fe. The results suggest that ligand dissociation leads to the  $C_{4v}$  symmetry as the most stable intermediate of the Fe during OER. This implies that Fe has a weakly coordinated or easily dissociable ligand that could serve to coordinate the O-O bond formation and, tentatively, play an active role in the  $Ni_x(Fe_{1-x})O_vH_z$  electrocatalyst.

### INTRODUCTION

Electrochemical water splitting  $(2H_2O \rightarrow 2H_2 + O_2)$  by renewable energy sources offers an attractive route toward carbon-free hydrogen (H<sub>2</sub>) production for application in, e.g., the transportation and energy sectors, as well as the chemical industry. 1,2 A remaining barrier to large-scale production of affordable clean hydrogen is that the anodic oxygen evolution reaction (OER) requires rare and expensive noble metal catalysts to overcome the slow kinetics resulting in increased costs for energy-efficient catalysts.3 Under alkaline conditions, iron-doped nickel (oxy)hydroxides,  $Ni_x(Fe_{1-x})O_vH_z$ , are among the most promising emerging OER electrocatalysts with excellent performance<sup>4–8</sup> compared to other nonprecious metal-based catalysts. Fe is essential for the catalytic activity of the material, but its exact role and character during operation remains elusive.

In general, nickel (oxy)hydroxides belong to a class of twodimensional dimensional hydrotalcite-like clay materials known as layered double hydroxides.9 These have a flexible chemical composition, with or without an intercalating layer of aqueous cations or anions, and where the structure can harbor a broad range of metal centers of different oxidation states from M(II) to M(IV). Fe-free, undoped NiO, Hz is a rather poor OER catalyst. However, incorporation of Fe ions to form  $Ni_x(Fe_{1-x})O_vH_z$  catalysts yields one of the most active alkaline

OER catalysts reported based on nonprecious elements, with optimal performance found for a 20-40% Fe content.<sup>4,5,8</sup> Catalytic OER current density of 10 mA cm<sup>-2</sup> can be reached at ~0.3 V overpotential in pH 13-14 in KOH electrolyte, although a decrease in overpotential and improvements in the long term stability are still needed for industrial feasibility.

A key to such further advancements is the understanding how Fe enhances the OER activity of the parent catalyst. This is a highly active research field with sometimes seemingly conflicting findings. 11-17 Various factors have been examined and advocated, including Fe as the active center, 18,19 Fe as a promotor of Ni active sites,<sup>20</sup> and a bifunctional active site comprising both Fe and Ni. 21 Computational studies investigating the roles of Ni versus Fe, as well as the significance of defects at edge, corner, and bulk active sites, have progressively provided more detailed mechanistic insights. 14,16,18,22-29 Yet, a consensus about the exact role and character of Fe under operation still eludes the field. The

Received: September 25, 2024 Revised: January 10, 2025 Accepted: January 10, 2025 Published: January 25, 2025





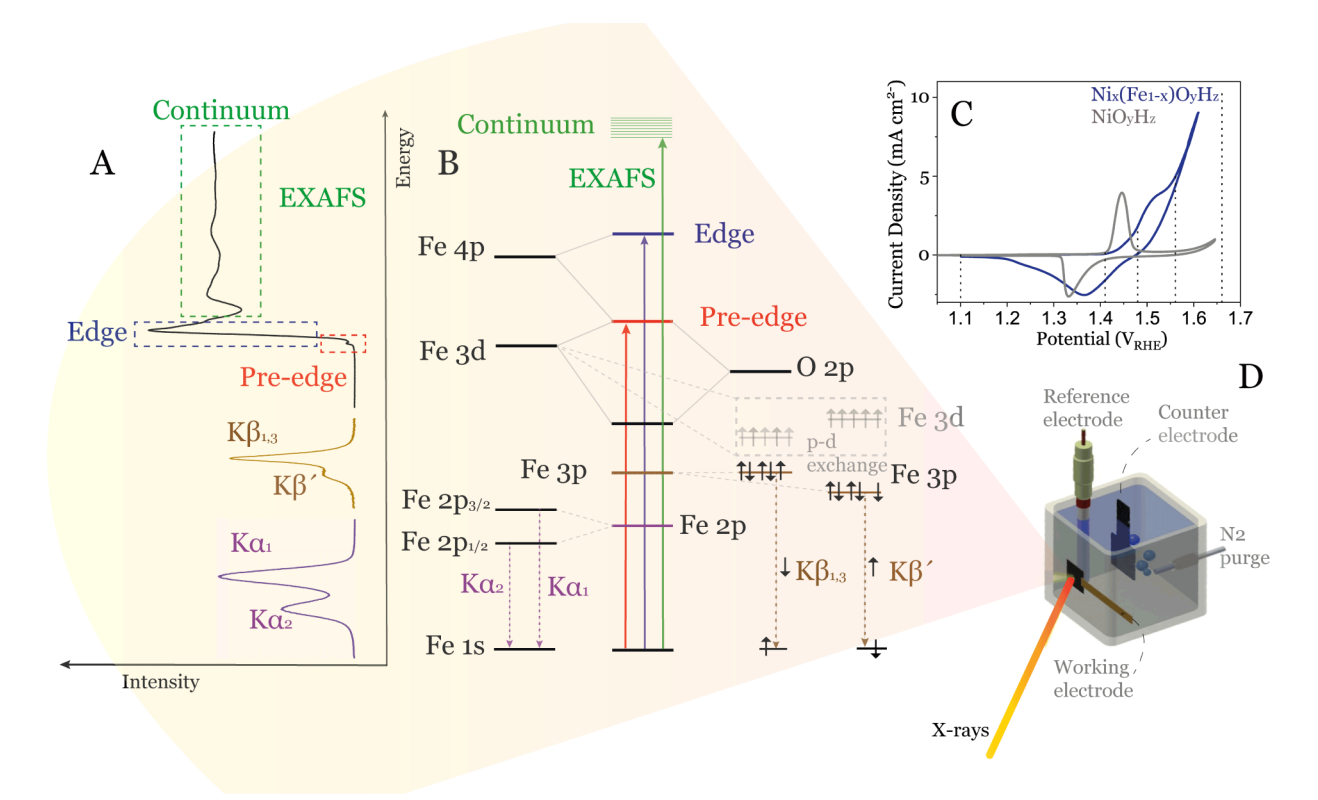


Figure 1. (A) Example Fe K-edge X-ray absorption data with pre-edge, edge, and EXAFS regions and spectral shape of  $K\beta$  main and  $K\alpha$  emission lines. (B) Simplified diagram of transitions that contribute to Fe K-edge XAS as well as Fe  $K\beta$  and  $K\alpha$  XES. (C) Polarization curve showing electrocatalytic OER performance for Ni<sub>x</sub>(Fe<sub>1-x</sub>)O<sub>y</sub>H<sub>z</sub> sample (blue) compared to NiO<sub>y</sub>H<sub>z</sub> (gray). Dotted vertical lines indicate potentials where operando X-ray data were collected. (D) Schematic view of the electrochemical cell for operando X-ray experiments.

disagreement over fundamental aspects, such as the oxidation state or local structure of the Fe site at catalytic conditions, highlights the challenges in probing Fe during its operational state. Numerous contradictory studies provide evidence that Fe ions either are electrochemically oxidized to  $Fe(IV)^{30}$ Fe(>IV),<sup>31</sup> or remain Fe(III)<sup>18</sup> under catalytic conditions. Structurally, Fe has been proposed to remain in the octahedral  $(O_{\rm h})$  coordination of the NiO<sub>v</sub>H<sub>z</sub> scaffold, <sup>32</sup> or to undergo reconstruction to square pyramidal  $(C_{4v})$ , planar, or tetrahedral  $(T_d)$  coordination structure upon the loss of one or two ligands forming Fe(V) and Fe(VI) respectively.<sup>31</sup> Fe has also been proposed to be a dynamic center, switching between a dissolved and immobilized state. 19 In addition, it remains unclear whether Fe is perfectly integrated into the  $NiO_vH_z$  or forms local FeO<sub>v</sub>H<sub>z</sub> patches with high Fe concentration. <sup>18</sup> The available literature on these proposals provides little conclusive evidence in either direction.

In situ experimentation has significantly been aided by improvements in instrumentation, sample environment cells, and light sources over the last decades. This has made it possible to employ X-ray spectroscopy techniques for probing (electro-)catalysts under operation with a high level of detail. Significantly For instance, K-edge X-ray absorption spectroscopy (XAS) using high-energy resolution fluorescence detection (HERFD) has been used to reveal the character of Co in the LiCoO<sub>2</sub> cathode of Li-batteries, significantly as well as in the alkaline water splitting catalysts for CoOOH, significantly MnO<sub>x</sub>, significantly been aided by improving the last of the Ni site in Ni<sub>x</sub>(Fe<sub>1-x</sub>)O<sub>y</sub>H<sub>z</sub>. Extended X-ray absorption fine structure (EXAFS) significantly been aided by improvement to the Ni site in Ni<sub>x</sub>(Fe<sub>1-x</sub>)O<sub>y</sub>H<sub>z</sub>. Extended X-ray absorption fine structure (EXAFS) significantly been aided by improvement to the last decades. This has made it possible to expect the last decades. This has made it possible to expect the last decades. This has made it possible to extend the last decades. This has made it possible to expect the last decades. This has made it possible to expect the last decades. This has made it possible to expect the last decades. This has made it possible to expect the last decades. This has made it possible to expect the last decades. This has made it possible to expect the last decades. This has made it possible to expect the last decades. This has made it possible to expect the last decades. This has made it possible to expect the last decades. This has made it possible to expect the last decades. This has made it possible to expect the last decades. This has made it possible to expect the last decades. This has made it possible to expect the last decades. This has made it possible to expect the last decades. This has made it possible to expect the last decades. This has made it possible to expect the last decades. This has made it possible to expect the last decades. This has made it pos

widely used to probe the character of transition metal centers under operation.

Here, we combine various operando X-ray spectroscopy techniques, encompassing HERFD, EXAFS, as well as  $K\alpha$  and  $K\beta$  XES, with density functional theory (DFT) simulations, including spectra simulation, to gain knowledge about the Fesite in the  $\mathrm{Ni}_x(\mathrm{Fe}_{1-x})\mathrm{O}_y\mathrm{H}_z$  electrocatalyst under OER operating conditions. Our results enable the assignment of characteristic spectral changes with reversible electronic and structural alterations of Fe as the applied potential bias is cycled from a resting (1.10  $V_{\mathrm{RHE}}$ ) to an operational (1.66  $V_{\mathrm{RHE}}$ ) state of the catalyst material. Whereas transient states of Fe under the catalytic cycle cannot be probed, the results show that the equilibrium structure of Fe remains Fe(III) under catalytic conditions with a  $C_{4v}$  Fe coordination as a likely key structure in the catalytic OER cycle.

Conceptual Background of the X-ray Spectroscopy (XAS and XES) Techniques. An X-ray absorption spectrum is obtained when a core electron is supplied with sufficient X-ray energy to be excited to the unoccupied states. XAS can be divided into different regions depending on the energy of the receiving states, see Figure 1. 33,34 Excitation into the lowest lying (valence/conduction band) electronic states is called the X-ray adsorption near edge structure (XANES) region. In Fe X-ray absorption spectroscopy, with partially occupied 3d-orbitals, XANES is subdivided into the "pre-edge" region (dashed red box in Figure 1A), which corresponds to weak, electric dipole-forbidden but quadrupole-allowed excitations 48,49 of the 1s core electrons into valence 3d and charge transfer levels (Figure 1B). These weak transitions can gain intensity via d-p mixing; see below. 33,34,50,51 The pre-edge is

sensitive to changes in the local coordination environment and oxidation state of Fe.  $^{33,34,43,52}$  The main edge (dashed blue box in Figure 1A) arises primarily from the dipole-allowed Fe 1s to 4p transition (Figure 1B) and reflects the effective nuclear charge  $(Z_{\rm eff})$  of Fe.  $^{33,34,53}$ 

When the atom absorbs enough energy such that a core electron can be emitted into the continuum (beyond the Rydberg states), the resulting photoelectron undergoes a complex sequence of scattering interactions with the neighboring atoms, resulting in the so-called extended X-ray adsorption fine structure (EXAFS) region (dashed green box in Figure 1A). This region can be used to determine the local geometric structure around the excited atom. A Fourier transformation of this spectral region yields information on the type of and distance to the neighboring atoms. <sup>33,34,51</sup>

In X-ray emission spectroscopy, XES, the core hole that was created in the X-ray absorption process, is filled by electrons from higher energetic orbitals.  $K\alpha$  (purple spectrum in Figure 1A) and  $K\beta$  mainline (i.e.,  $K\beta_{1,3}$  and  $K\beta$ , brown spectrum in Figure 1A) emissions have the same fluorescence initial states with an 1s vacancy, but in  $K\alpha$  and  $K\beta$  emissions this vacancy is filled by 2p or 3p electrons, respectively (Figure 1B). The overall spectral shape of the  $K\beta$  emission is dominated by the (3p, 3d) exchange interaction (Figure 1B), making it extremely sensitive to oxidation and spin state changes, while the 2p spin—orbit splitting shapes the  $K\alpha$  spectra. <sup>33,34,44,45</sup> Thus, an XANES spectrum reflects the unoccupied density of electronic states, while an XES spectrum is related to the density of occupied states. By using the X-ray techniques mentioned above, we aim to gain more complete insight into the role of Fe in  $Ni_x(Fe_{1-x})O_vH_z$  electrocatalyst under operando conditions at different electrochemical potentials. In the text below, we focus on the interpretation and discussion of the Fe site; however, corresponding data for the Ni site are included in the Supporting Information.

# ■ RESULTS AND DISCUSSION

Structural Information from EXAFS and Main-Edge **XANES.** Based on a previous report,<sup>29</sup> the  $Ni_x(Fe_{1-x})O_yH_z$ electrodeposition synthesis protocol employed herein yields layered structures with Ni and Fe centers in edge-sharing octahedral arrangements in accordance with the reported literature. 18,32,54 These layers have been reported to be separated by intercalating water and ions with a low degree of layer-to-layer long-range ordering which allows for catalytic activity to be distributed throughout the material. 5,9,32,55 Since the catalytic activity is not limited to the surface, bulk-sensitive techniques such as XAS can readily probe relevant active sites. To identify structural changes in the local environment of the  $Ni_x(Fe_{1-x})O_vH_z$  catalyst, operando EXAFS measurements were conducted in a 0.1 M KOH electrolyte starting from the resting state (+1.10 V<sub>RHE</sub>) followed by stepping the potential up to the OER catalytic state (+1.66 V<sub>RHE</sub>), and then back down to the resting state (see Figure 1C and EXAFS simulations using FEFF section in SI). We consider the EXAFS region of the spectrum (signal after Fourier transformation into R-space without phase correction), shown in Figure 2, for a quantitative assessment of the bonding arrangement. The Fe EXAFS spectrum at the resting state and potentials up to 1.48  $V_{RHE}$  displays two distinct peaks. Fitting these peaks with FEFF<sup>56</sup> and SimXLite<sup>29</sup> reveals octahedral-like coordination with average Fe-O and Fe-M bond lengths of 1.985  $\pm$  0.01 Å 3.050  $\pm$  0.019 Å, respectively.

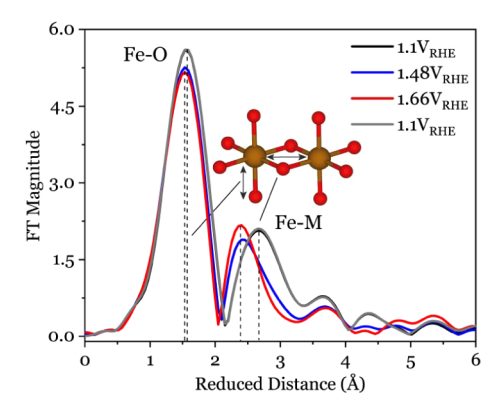


**Figure 2.** Fourier transformed EXAFS spectra of Fe K-edge for  $Ni_x(Fe_{1-x})O_yH_z$  a recorded *operando* at varied electrode biases.

These values align well with those reported in previous studies (Table S1).  $^{18,29,57}$  At potentials of +1.48  $V_{\rm RHE}$  and above, the EXAFS peaks shift toward shorter bond lengths without broadening either the Fe (Figure 2) or Ni (see Figure S3) spectral features. This indicates significant bond contraction without a significant change in site homogeneity. Fe–O bond lengths decrease from 1.985 Å (+1.10  $V_{\rm RHE})$  to 1.940 Å (+1.48  $V_{\rm RHE})$  and remain the same (1.938 Å) at the highest applied potential (+1.66  $V_{\rm RHE})$ . Notably, these bonds expand to 1.997 Å upon returning to the resting state potential (+1.10  $V_{\rm RHE})$ , confirming reversibility (Figure 2).

A strong correlation was observed not only between Fe–O and Ni–O bond lengths (Figures S1–S3) but also between nearest metal–metal distances, which decrease from 3.050 Å (+1.10  $V_{RHE}$ ) to 2.889 Å (+1.66  $V_{RHE}$ ). This agrees well with previous in situ EXAFS studies reporting contraction in the local metal–O and metal–metal distances. <sup>29,37,57</sup> Shorter bond distances is usually associated with increased oxidation state or changes in structural symmetry/geometry. <sup>41,42</sup> However, the absence of a Fe K-edge energy shift to higher energies (Figure 4A) has casted doubt on an increase in the Fe oxidation state (from +3 to +4) despite the short Fe–O bond. This contraction may just be a response to the contraction in the NiO<sub>v</sub>H<sub>z</sub> host lattice, which will be further explored below.

To quantify the changes observed at different applied potentials, EXAFS fits using the FEFF multiple scattering approaches were performed for both the Fe and Ni K-edges, assuming layered Fe-doped structures (see Section S4). The fits employed DFT optimized structures (Figure S5, Table S3 and S4) of NiO<sub>2</sub>,  $\beta$ -,  $\gamma$ -NiOOH,  $\alpha$ -,  $\beta$ -Ni(OH)<sub>2</sub>, with 25% Fe doping, which are presented in Figures S7 and S8. As discussed in the Supporting Information, satisfactory fits for the least anodic potential (+1.10 V<sub>RHE</sub>) were achieved with a linear combination fit primarily using  $\alpha$ -,  $\beta$ - Ni(OH)<sub>2</sub> with Fe<sup>3+</sup>Ni<sup>2+</sup> and  $\beta$ -NiOOH with Fe<sup>3+</sup>Ni<sup>3+</sup>structures (Figures S6–S7 and Table S5). For the most anodic potential (+1.66  $V_{RHE}$ ), the best fits were obtained with DFT-optimized structures containing 26% of  $\beta$ -NiOOH- Fe<sup>3+</sup>Ni<sup>3+</sup> (where Fe is in the distorted  $O_h$  symmetry) and 37% of  $\gamma$ -NiOOH-Fe<sup>3+</sup>Ni<sup>4+</sup> (with Fe in 5-fold coordinated  $C_{4v}$  symmetry). These EXAFS fits support the distorted  $\gamma$ -NiOOH structure at the most oxidizing potentials and a more well-ordered Ni(OH)<sub>2</sub> structure at resting state potentials. We want to stress, therefore, that all fitted structures have Fe in the 3+ oxidation state. The coexistence of Fe3+ in different local geometries is further supported by minor energy difference (2-3 meV per

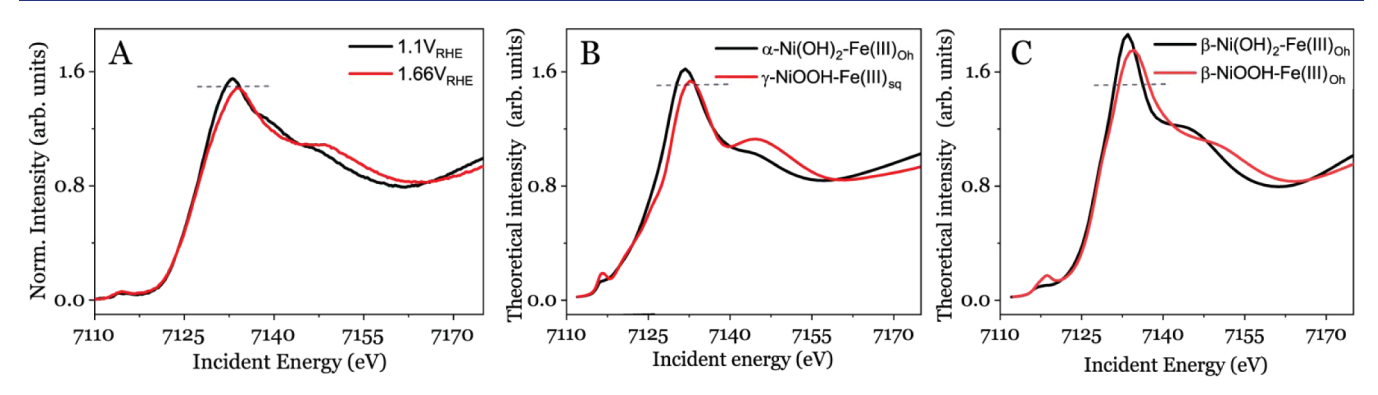


Figure 3. Operando experimental (A) and FEFF simulated (B and C) Fe K-edge XAS spectra for different applied potentials The dashed horizontal line guides the eye to the intensity level of the experimentally observed while line at 1.1 V RHE.

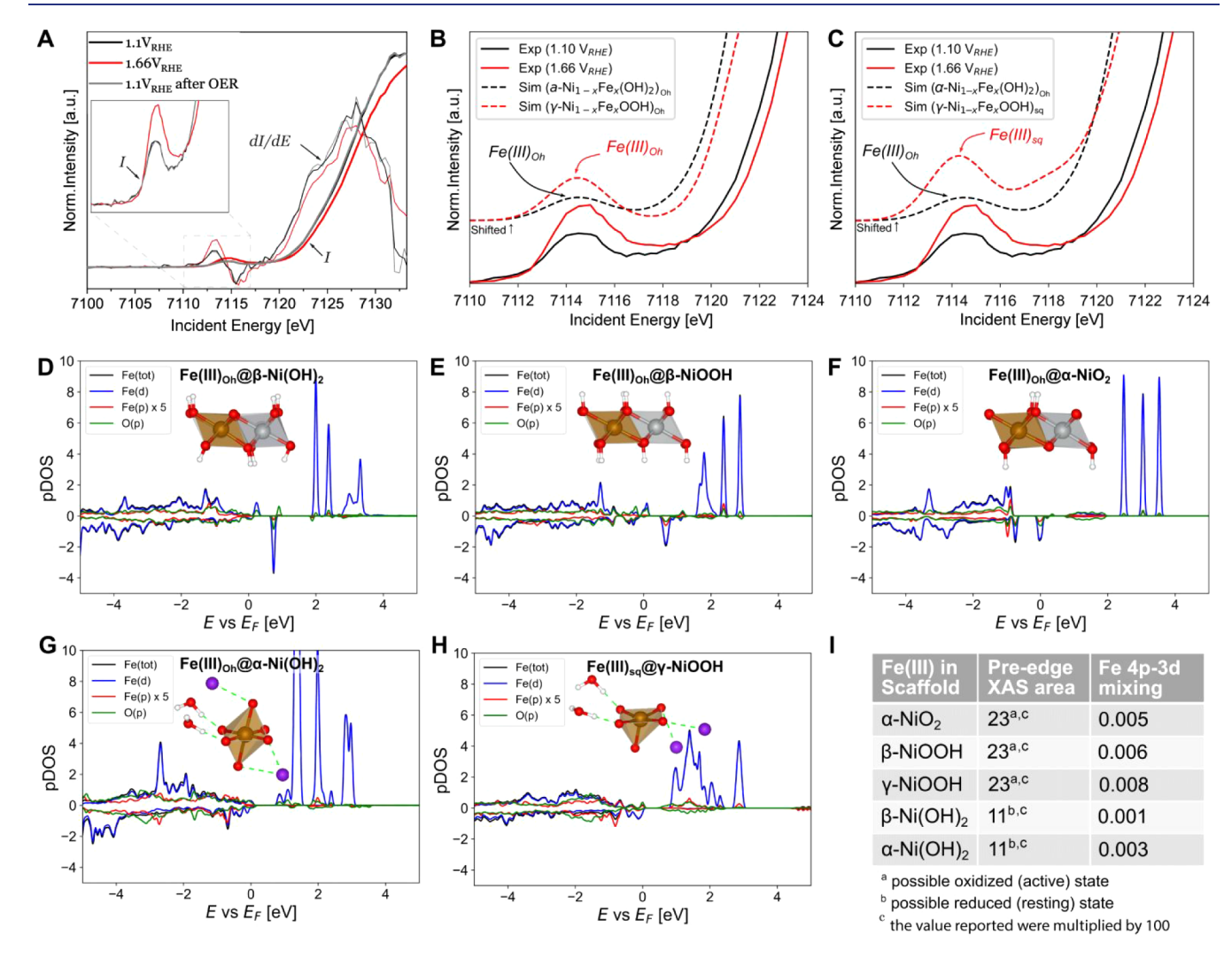


Figure 4. (A) The experimental and first derivative of the normalized XANES data. (B–C) DFT-simulated versus experimental pre-edge XAS. The simulated spectra have been shifted for clarity. (D-H) Core hole density of states (DOS) computed for dilute Fe(III) in different NiO<sub> $_{y}$ </sub>H<sub> $_{z}$ </sub> environments. (I) Computed Fe 4p-3d mixing in the XAS valence pre-edge 4d acceptor states versus integrated pre-edge XAS peak area for Fe(III) in different NiO<sub> $_{y}$ </sub>H<sub> $_{z}$ </sub> environments. Normalized pre-edge area expressed in  $10^{-2}$  eV units.

Ni(Fe) $O_yH_z$  unit from DFT calculations) between  $\gamma$ -NiOOH with Fe<sup>3+</sup> in 5-fold coordinated  $C_{4\nu}$  geometry versus  $O_h$  coordination symmetry, indicating that this is a viable interpretation of the atomic structures. Based on these findings, a plausible explanation for the observed EXAFS spectral changes is the oxidation of the Ni scaffold from Ni<sup>2+</sup> in

 ${
m Ni(OH)_2}$  (at +1.10  ${
m V_{RHE}}$ ; resting state) to  ${
m Ni^{3+}/Ni^{4+}}$  in  $\gamma$ -NiOOH with enhanced structural distortion around Fe centers at oxidizing potentials (at 1.66  ${
m V_{RHE}}$ ; catalytic state).

Experimental XANES reference data is available only for a five-coordinate  $C_{4\nu}$  Fe molecular mononuclear complex with N,N,O-tridentate 3,3-bis(1-alkylimidazol-2-yl) propionate li-

gands, which mimic the active sites of dioxygenase enzymes. 58,59 However, these ligands differ from the catalytic intermediate proposed in this study. Therefore, we compare our results with simulated spectra, as they better represent the hypothesized structure compared to the reference structures available in the literature. Figure 3 shows measured and simulated XANES spectra for the structures from Figure S5, Tables S3 and S4. The simulated spectra are modeled using the FEFF software that employs a full multiple scattering approach, making it sensitive to the system geometry but less to the electronic structure (e.g., pre-edge features are typically not modeled well),<sup>56</sup> see Methods. A comparison of the simulated spectrum of  $\alpha$ -Ni(OH)<sub>2</sub> with Fe doping in  $O_h$  symmetry (Figure 3B) matches the intensity of the experimentally observed largest absorption peak (also known as the "white line") of the  $Ni_x(Fe_{1-x})O_yH_z$  in the resting state at 1.10  $V_{RHE}$ (Figure 3A). In contrast, the XANES spectra at  $+1.66 V_{RHE}$  in Figure 3A is best matched with the simulated spectra of  $\gamma$ -NiOOH doped with Fe in  $C_{4\nu}$  symmetry (Figure 3B). This result can, e.g., be realized from the predicted intensity attenuation of the white line and a shift of it to higher energy in the simulated spectra of  $\gamma$ -Ni (Fe)OOH in Figure 3B, which agrees well with the measured XANES spectrum (Figure 3A). This observation aligns well with a modification of the coordination environment of Fe ions occurring at +1.66 V<sub>RHE</sub>. Consistent with the EXAFS data, these XANES results suggest that the observed structural changes involve the shortening of the Fe-O (1.938 Å) and Fe-Ni (2.887 Å) distances. The FEFF-simulated spectra in Figure 3C fit to the experimental observation in Figure 3A but to a lesser degree than Figure 3B due to the broader and more intense "white line" in Figure 3C.

In summary, the Fe-O bond length (1.938 Å) at 1.66 V<sub>RHE</sub> found through the EXAFS analysis is short for Fe(III), even in a distorted  $O_h$  geometry. However, the absence of an expected shift to higher energy for both the pre-edge centroid (Figure 4A) and the main edge suggests that the formation of Fe(IV) is unlikely.60-62 Instead, the experimental observations (Figures 2 and 3A, and discussion below) could be explained by the loss of one Fe-O bond.<sup>50</sup> This decrease in coordination number would perturb the symmetry of the site and break the centrosymmetry, leading to geometric transformation from 6fold coordinated  $O_h$  symmetry to 5-fold coordinated  $C_{4\nu}$ symmetry. Consequently, the five remaining Fe-O bonds would contract. While EXAFS accurately provides information regarding first-shell Fe-O distances, it determines coordination numbers with the inherent uncertainty of approximately 20% and provides limited information on the site geometry. 63,64 However, shorter bonds in lower coordination complexes<sup>65–68</sup> also contribute to increased 4p mixing.<sup>50,69</sup> Therefore, in the next section, we explore in more detail how the electronic structure of various  $Ni_x(Fe_{1-x})O_yH_z$  states corresponds to changes in the pre-edge XANES spectra, which are sensitive to both the oxidation state and the geometry of the Fe atoms. 69-7

Analysis of the Adsorption Pre-Edge by HERFD XAS. Probing the XAS pre-edge region of transition-metal centers has been demonstrated as a versatile tool for examining the electronic structure of electrocatalysts *in situ*. <sup>35,72</sup> In general, the pre-edge energy position is determined by the energy of the metal *d*-band states and the core 1s orbital, while the main edge position relates the energy between the Fe 1s and 4p orbitals. A linear relationship has been found between both the

edge and pre-edge positions with atomic charge as well as effective nuclear charge  $(Z_{\rm eff})^{.51,60}$  Therefore, the oxidation state change of the absorbing metal center, which is closely tied to  $Z_{\rm eff}$  directly affects the energy positions of the edge and the pre-edge. For instance, since  $Z_{\rm eff}$  of the absorbing atom typically increases if oxidation occurs, both the edge and the pre-edge will shift to higher energy. This is because the 1s core level states experience a stronger influence from changes in  $Z_{\text{eff}}$ relative to the more weakly bound and more screened valence states. As  $Z_{\rm eff}$  increases, the energy gap between the core and the valence level increases resulting in shifts of the pre-edge and the rising edge to higher energies. Contracted bond distances observed in the EXAFS (Figure 2) are commonly associated with an increased oxidation state. Such oxidation state increases might also be seen in the Fe XANES spectra, where the fine structure of the peaks contains valuable information about the electronic states of the sample.

Fe K-edge (1s to 3d or 4p transitions) XANES has been extensively employed to probe electronic structural changes in OER electrocatalysts. However, with traditional XANES methods, the short 1s core hole lifetime  $^{73,74}$  leads to spectral broadening and a loss of chemical information. This limitation can be overcome by using high-energy resolution fluorescence detected (HERFD) XANES. Systems By selectively measuring the  $K\alpha_1$  fluorescence line  $(2p_{3/2} \rightarrow 1s)$  using high-resolution Bragg optics, the effective broadening of the 1s core hole lifetime can be suppressed. Employing this technique, the chemical information lost in the TFY (Total Fluorescence Yield) spectrum can be recovered, as demonstrated in the HERFD Fe spectrum in Figure S9.

Fe HERFD recorded at potentials ranging from  $+1.10 \text{ V}_{\text{RHE}}$ to +1.66  $V_{\text{RHE}}$  are presented in Figure 4A. The pre-edge features do not change their energy positions, which is strikingly different from previous experimental observations for Fe complexes in various oxidation states and, notably different from oxidation of the Fe from Fe(II) to Fe(III) or Fe(IV).60,62,79-81 As for the pre-edge, the energy position of the main edge remains constant between +1.10  $V_{\text{RHE}}$  and +1.66 V<sub>RHE</sub> potentials (inflection points in the first derivative of the normalized HERFD data Figure 4A), as also seen in the literature. Accordingly,  $Z_{\text{eff}}$  is constant in contrast to what is expected upon oxidation of the Fe centers. This observation corroborates our interpretation that spectral changes seen for different potentials are associated with changes in the ligand field around Fe centers, resulting in ligand field splitting caused by local geometric variations. If an oxidation state change occurred, the change in Z<sub>eff</sub> would have needed to affect the energy of the 1s and 4p states to a similar degree in order to match the obtained HERFD spectra, which is possible but highly unlikely.

The 1s-3d pre-edge feature is also sensitive to the ligand geometry around the Fe center. Generally, a larger pre-edge intensity with no change in energy positions is associated either with (i) symmetry distortion due to deviation from the centrosymmetric coordination environment leading to asymmetric bond lengths or (ii) a decrease in coordination number from the centrosymmetric  $O_h$  with a decrease in the coordination number. In the latter case, the rule of thumb postulates that the  $O_h$  (6-coordinated) environment corresponds to the weakest pre-edge intensity with increasing intensity for lower coordination numbers (see inset Figure 4A–C). <sup>44,50,60,69,71</sup> As the symmetry becomes more distorted, the pre-edge peak area increases. This increase in intensity is

assigned to mixing metal 4p into the 3d orbitals, which adds some dipole-allowed 4p character to the usually dipole forbidden (but quadrupole allowed) pre-edge transition (1s-3d+4p transition with d-p mixing). This yields an increased intensity even at small admixtures, since electric quadrupoleallowed transitions are about 100-times weaker than electric dipole-allowed transitions.<sup>48</sup> As a result, only a few percent of 4p mixing into the 3d orbitals can significantly impact the intensity of the 1s-3d pre-edge feature. This correlation has been utilized in numerous studies, not only for Fe, 50,69,71 but also for other transition metals, such as Mn, Co, Ni, and Cu, in relation to their geometry and coordination number. 53,82-84

In a centrosymmetric six-coordinated environment, 1s-3d pre-edge intensity can only be due to the weak electric quadrupole mechanism since mixing of the gerade 3d orbitals with the ungerade 4p orbitals is not allowed. From previous work, the pre-edge intensity of 23  $O_h$  Fe(III) complexes,  $^{50,69}$  is on average 6.2 eV units (note that here and below normalized pre-edge area expressed in 10<sup>-2</sup> eV units) with the postedge continuum normalized to unity. The pre-edge here consists of two features split by the crystal field parameter 10Dq. Since in high spin Fe(III), the five d-electrons each singly occupy the orbitals, the ground state spectroscopic term <sup>5</sup>A<sub>1g</sub> has a  $(t_{2g})^3(e_g)^2$  character that produces two excited hole configurations  $(t_{2g})^2(e_g)^2$  and  $(t_{2g})^3(e_g)^1$  upon promotion of 1s into 3d unoccupied states. This results in final states of  ${}^5T_2$  and  ${}^5E$ characters (i.e., two peaks split by 10Dq), respectively, as observed in previous studies. S0,85-87 In contrast, the pre-edge area observed for the resting state of the  $Ni_x(Fe_{1-x})O_yH_z$ catalysts at a potential of 1.10 V<sub>RHE</sub> is equal to 11 units and does not have a pronounced multiplicity of the peak. This experimental observation of increased area can be adequately explained from 4p mixing into 3d orbitals, leading to a gain of intensity through additional electric dipole transitions. Assuming that the pre-edge area of 6.2 units (as determined from the  $O_h$  Fe(III) complexes, see above) represents the total quadrupole intensity, the remaining pre-edge area in the  $Ni_x(Fe_{1-x})O_yH_z$  at a potential 1.1  $V_{RHE}$  should be attributed to the amount of electric dipole intensity. Therefore, the dipole intensity of the pre-edge feature can be estimated to be 4.8 units (11-6.2), which originates from the 4p character in the 3d orbitals. The relationship between the intensity of dipole contribution to the pre-edge intensity and the amount of 4p character in the final state for Fe(III) is well established and corresponds to 1.5 units for a 1% increase in Fe(III) 4p character. Therefore, the contribution of Fe 4p character to the unoccupied valence 3d orbitals is estimated to be 4.8/ 1.5 = 3.2% for  $Ni_x(Fe_{1-x})O_vH_z$  at potential 1.10  $V_{RHE}$ .

Both dimetal Fe(III) oxides 44 and six-coordinate  $\mu$ -oxobridged dimetallic Fe(III) complexes<sup>50,69</sup> also exhibit similar single pre-edge structure and a similarly sized area within the range of resting state of  $Ni_x(Fe_{1-x})O_vH_z$  at a potential of 1.10 V<sub>RHE</sub>. The interpretation there is that the Fe site has distorted Oh symmetry and the distribution is understood by invoking 3*d*-4*p* mixing into the orbital component along the distortion. The inversion symmetry is broken and allows mixing between the 3d and the 4p orbitals (both axial distortions along the zaxis and the equatorial plane permit mixing of the same symmetry 3d and 4p orbitals and are allowed to mix by the group theory).  $^{50,85-87}$ 

The pre-edge gains intensity by a factor of ~2 upon applying OER potentials (areas at +1.10  $V_{RHE}$  = 11 and +1.66  $V_{RHE}$  = 23). This indicates a significantly more covalent bonding at

+1.66  $V_{RHE}$  and even more increased 3d-4p mixing than in the resting state potential of +1.10 V<sub>RHE</sub>. Based on the assumption stated earlier, the percentage of Fe 4p mixing into the Fe 3d orbitals is thus estimated to be (23-6.2)/1.5 = 11.2% for OER active  $Ni_x(Fe_{1-x})O_vH_z$ . A plausible explanation for the gain in pre-edge intensity at +1.66 V<sub>RHE</sub> compared to +1.10 V<sub>RHE</sub> without a shift to higher energy is a geometric transformation from distorted six-coordinated sites to a five-coordinated environment or to a mixed state with both five- and sixcoordinated Fe. Such explanations also find support in the literature 50,69

The loss of a ligand increases the amount of total 4p mixing in Fe(III) complexes (experimentally determined 4p character at  $+1.10 \text{ V}_{\text{RHE}} = 3.2\%$  and  $+1.66 \text{ V}_{\text{RHE}} = 11.2\%$ ) and is attributable to the generally shorter bond lengths, thereby accentuating geometric perturbations. A shorter Fe-O bond correlates with the decrease in coordination number, which is associated with a larger mixing of Fe 4p states into the Fe 3d orbitals, and gives rise to an electric dipole that allows Fe 1s-3d +4p transition at +1.66 V<sub>RHE</sub>. This correlation is also supported by the EXAFS data in Figure 2.

To further investigate the origin of the spectral features of the pre-edge, DFT-simulated XAS spectra were computed for a library of structures containing Fe in various environments (Figure 4B,C). In this way, plausible structural environments can be tested with the best fits kept for further evaluation. The encompassed structures are based on  $\alpha$ -, $\beta$ -Ni(OH)<sub>2</sub>,  $\beta$ -, $\gamma$ -NiOOH, and  $\alpha$ -NiO $_2$  with doped Fe forged into symmetric and asymmetric  $O_h$ ,  $C_{4v}$ , and  $T_d$  (shown in Figures S10–S12). Ligand environments within the NiO<sub>v</sub>H<sub>z</sub> scaffold structures were further varied by either adjusting O/OH group ratio (thus allowing for variation of the local oxidation state from II to IV), or by substituting one O/OH group by water, epoxide, or peroxide groups. The full data set is presented in the SI. At the resting state of the catalysts, the best fits versus experimental pre-edge data is found for a high-spin Fe(III) oxidation state in a local  $FeO_3(OH)_3$   $O_h$  coordination environment within an  $\alpha$ -Ni(OH)<sub>2</sub> scaffold (Figure 4B,C). An Fe(III) center in a distorted  $O_h$  FeO<sub>3</sub>(OH)<sub>3</sub> coordination, but residing within a  $\gamma$ -NiOOH scaffold, also provided a reasonable match for the data representing the catalytically active state (Figure 4B). Nevertheless, for the data acquired at +1.66 V<sub>RHE</sub>, a closer match between experiment and simulations was found for a  $C_{4\nu}$  FeO<sub>4</sub>(OH)<sub>1</sub> coordination around a Fe (III) center (Figure 4C).

Following the procedure of Juhlin et al.,36 who studied preedge features of Co in LiCoO2, we can further investigate the origin of the pre-edge for Fe(III) by decomposing the peak into dipolar and quadrupolar components. Although both components give non-negligible contributions, the dipole contributions explain the majority of the peak (as noted above). The dipolar transition becomes allowed due to the significant mixing of the 3d Fe with the Fe 4p states and, to a lesser extent, the O 2p states (see Figure 4D-H). For the oxidized  $Ni_x(Fe_{1-x})O_vH_z$  structures at OER conditions, the p-d mixing effect is enhanced by the asymmetry introduced by the 5-fold coordination environment with mixed O and OH ligands. In addition, the effect becomes more apparent as the NiO<sub>v</sub>H<sub>z</sub> scaffold surrounding the Fe(III) site becomes further oxidized, leading to a Fe-O bond contraction. In other words, in line with the experimental results discussed above and ligand field theory, the covalency increases as the catalyst shifts from its resting to active state. Consequently, the amount of Fe 4p

and O 2*p* mixing in the Fe 3*d*-dominated band gap state close to the Fermi-level scales with the area under the pre-edge peak (see Figure 4I). The larger *p*-mixing (cf., Figure 4H) observed in the active states results in a larger pre-edge area (Figure 4I).

Spin State and Effective Core Potential Probed by the XES K-Edge Spectra. To further validate our interpretation of the HERFD XAS data, we employ XES spectroscopy to probe both the K $\alpha$  and K $\beta$  emissions. Together, the XES spectra serve as a robust test for the consistency of our hypothesis, which suggests a nonoxidative local structural change in the Fe geometry. The  $K\alpha$  XES probes the 2p to 1s transition and is split into  $K\alpha_1$  and  $K\alpha_2$  peaks due to spin-orbit interactions. It was reported that the full width at half-maximum (fwhm) of the  $K\alpha_1$  line is roughly proportional to the "nominal" number of unpaired 3d electrons, <sup>88–91</sup> i.e., the number of unpaired 3d electrons as derived from the formal oxidation state of the metal atom. This proportionality is usually explained within the framework of multiplet theory by assuming that the  $K\alpha_1$  line is broadened by the exchange interaction between the 2p hole in the final state and the populated 3d orbitals. Therefore, it reflects the net spin located at the metal atom. However, the 2p-3d exchange interaction is weaker than the spin-orbit interaction of the 2p level and the spin-polarized nature in  $K\alpha$  is manifested as a slight asymmetry hidden within the single  $K\alpha_1$  and  $K\alpha_2$ peaks. 44,45 Nonetheless, a roughly linear relation between the fwhm of the more intense  $K\alpha_1$  peak and the nominal spin value given by the 3d electrons has been established. 44,45,8

It is known that Fe-sites remain as high spin Fe(III) (S = 5/2) below the oxidation threshold potential of Ni(OH)<sub>2</sub>/NiOOH at ~1.35 V<sub>RHE</sub>.  $^{30,41}$  High-spin Fe(II) and Fe(IV) both have a S = 2 spin state. Thus, if the Fe transitions to a different spin or oxidation state occur leading to a change in the number of unpaired 3d electrons, it would be reflected in the fwhm of the  $K\alpha$  XES spectra. As seen in Figure 5A comparing the Fe  $K\alpha$  XES spectra at 1.10 and 1.66 V<sub>RHE</sub>, no spectral change associated with a change in oxidation or spin state is noted. This again suggests that the spectral changes seen in the XANES and EXAFS spectra (Figures 2, 3A and 4A) are not related to oxidation nor spin state changes and that Fe remains in the same state within the considered potential range. Instead,  $K\alpha$  spectra is in line with previously reported effects of geometry changes for high-spin Fe(III) complexes.  $^{44}$ 

The relative peak shape and position of the  $K\beta$  fluorescence transition (3p to 1s) is dominated by the 3p-3d exchange interaction that is stronger than the 2p-3d interactions of  $K\alpha$  XES. This makes  $K\beta$  XES much more sensitive to local spin magnetic moments in the 3d shell as well as changes in the number of unpaired 3d electrons than the  $K\alpha$  XES. The  $K\beta$  spectrum comprises a main intense peak,  $K\beta_{1,3}$ , and a low energy shoulder,  $K\beta$ . Whereas the main peak  $K\beta_{1,3}$  mainly reflects transitions from 3p that have spin-states of opposite direction to the majority of the 3d spin states, the satellite  $K\beta$  arises from transitions from states of the same spin direction.

It is known that the main  $K\beta$  lines (as discussed in the Introduction) are much more sensitive to the metal spin and geometry state change than the  $K\alpha$  lines. In Figure 5B, we compare the spectra of  $Ni_x(Fe_{1-x})O_yH_z$  as a function of the applied potential. All spectra show Fe in high-spin states, which is concluded from the presence of the  $K\beta'$  feature that would otherwise shift to higher energies and merge with the main feature around the  $K\beta_{1,3}$  peak for low-spin states due to the weak 3d spin moment. At the potential of 1.48  $V_{RHE}$  Figure 2

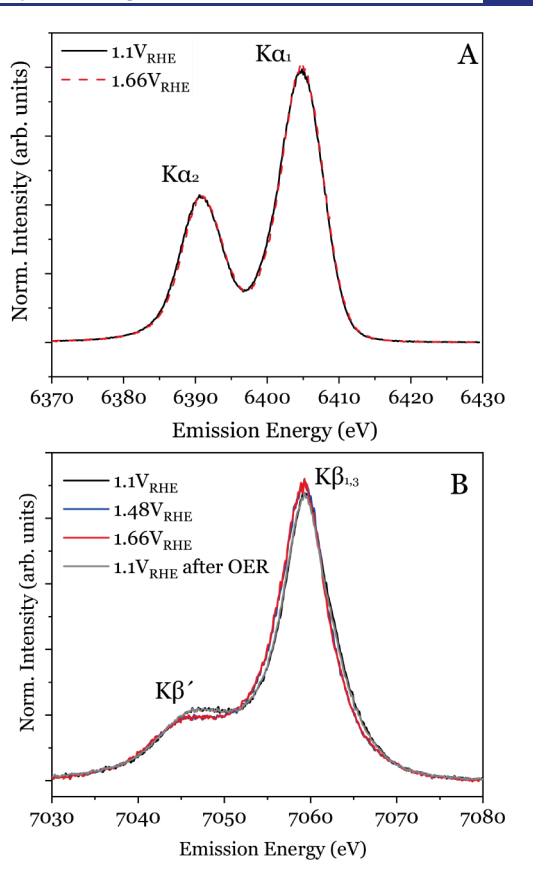


**Figure 5.** (A) Fe Kα XES spectra of  $Ni_x(Fe_{1-x})O_yH_z$  at 1.10 and 1.66  $V_{RHE}$ . (B) Fe Kβ main line XES spectra of  $Ni_x(Fe_{1-x})O_yH_z$  cycled from 1.10  $V_{RHE}$  to 1.66  $V_{RHE}$  and back to 1.10  $V_{RHE}$  after OER. See Supporting Information for the full data set.

the  $K\beta$  spectra show a slightly less pronounced  $K\beta$  shoulder and the main  $K_{\beta 1,3}$  peak shift toward lower energy with respect to the potentials below +1.48  $V_{RHE}$  (see Supporting Information for the full data set). The spectral signatures corresponding to the bond length contractions in the EXAFS data occur at the same potential here (Figure 2). Again, as in all the above experiments, the changes in the main  $K\beta$  lines are fully reversible.

It is a reasonable hypothesis to attribute the observed spectral changes to spin and/or oxidation state changes, as previously reported for Fe and other 3d transition metals  $^{44,45,88,93-95}$  To evaluate the  $K\beta$  spectral evolution, we have performed an IAD (Integrated absolute difference, see Figure S14) analysis.<sup>88</sup> As suggested by Glatzel and coworkers<sup>44</sup> this is carried out after aligning the spectra to have the same center of gravity (COG) to eliminate the energy shift due to the screening of the core-hole potential, which depends on the valence charge density. We assume the same high-spin  $3p^53d^5$  final state for all applied potentials. The resulting IAD analysis yields identical results with or without the COG alignment (Figure S14). This implies that the shift of the  $K_{\beta1,3}$ peak is not caused by variations in the electronic screening that arise from changes in the valence charge density between different oxidation or spin states but can be attributed almost entirely to the 3p-3d mixing.44

The following discussion provides further support for our interpretation of the constant formal Fe(III) oxidation state with changes occurring only through symmetry breaking and bond contraction around the Fe ion. As the splitting between

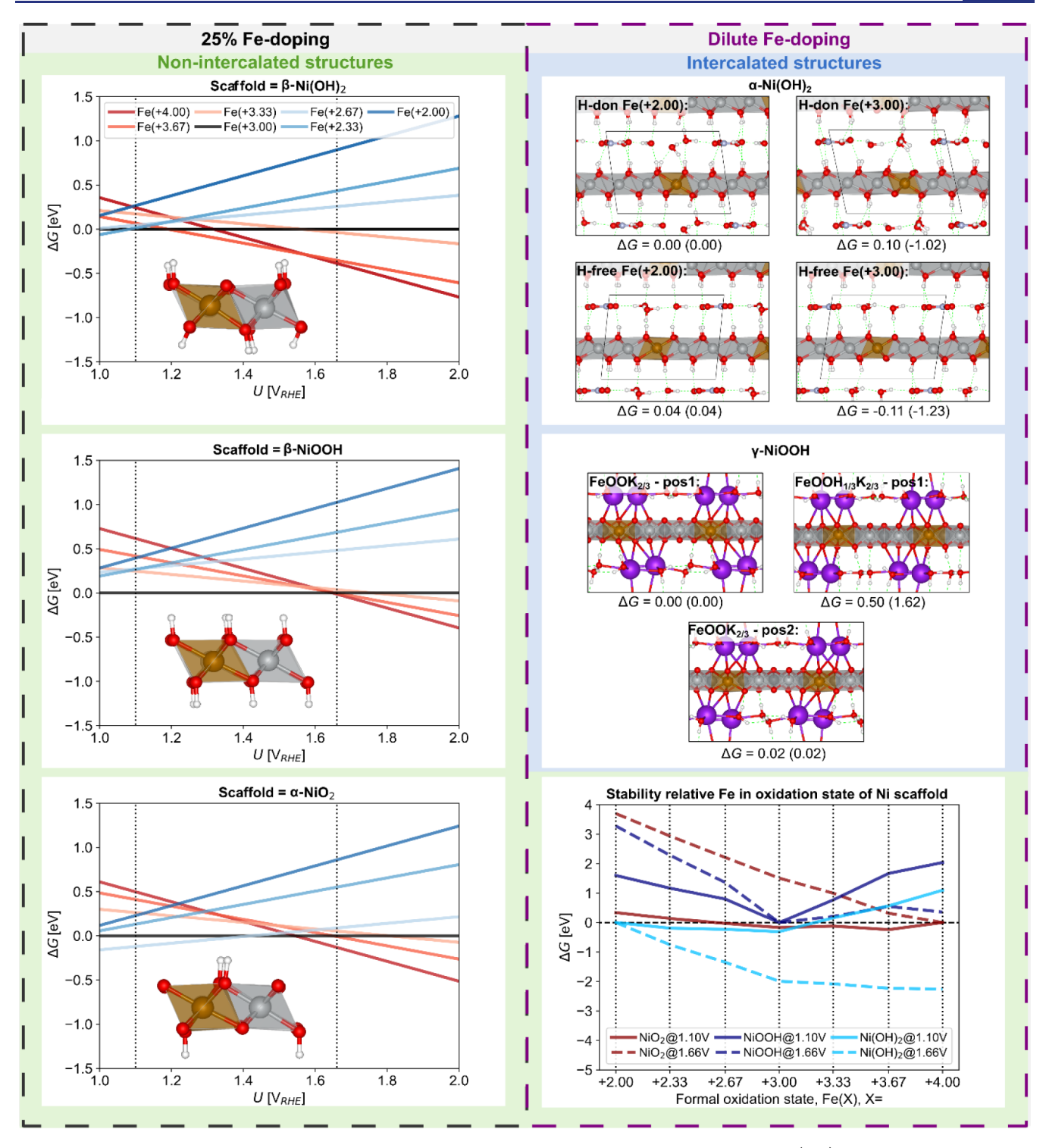


Figure 6. DFT optimized structures and relative energies. To the left, bulk free energies per metal unit ( $\Delta G$ ) of 25% Fe-doped NiO<sub>γ</sub>H<sub>z</sub> nonintercalated scaffold structures as a function of potential for varied Fe oxidation states. Inserts show a single layer of optimized Fe(III) structures. To the right, dilute Fe-doping. Top right, intercalating  $\alpha$ -Ni(OH)<sub>2</sub> with Fe doped at two different positions: "H-don" (H-donating) where all the OH groups are donating H-bonds to the intercalating water, and "H-free" where two OH are not participating in the H-bonding network. These energies correspond to Fe(II) are compared to Fe(III) structures with corresponding energies in brackets. Middle right, γ-NiOOH with Fe doping at two positions. Although this state is formally Fe(+3.67), its magnetic moment (4.25) and Bader charge (1.71) best corresponds to a Fe(+3.00) state. <sup>94</sup> These are compared to a structure with two added H, yielding a formal Fe(+3.00) state. Lower right, nonintercalating low Fe-doping (6%): relative free energy at resting and activated state potentials versus formal oxidation state.

the  $K\beta$  mainline features is governed largely by the 3p-3d exchange integrals, it has, e.g., been found that the split is modulated by the metal–ligand covalency for, e.g., Fe, Co, and Mn in both  $O_h$  and  $T_d$  coordination. Experimental

studies have reported a reduced  $K\beta'-K\beta_{1,3}$  splitting for Fe with an increase in the covalent character in the  $K\beta$  spectra of the compounds having the same nominal spin<sup>46,94</sup> The herein observed 0.1 eV shift in the first moment of the  $K\beta_{1,3}$  peak

between +1.10  $V_{RHE}$  and +1.48  $V_{RHE}$  (as shown Figure 5B, with details provided in the SI) is in agreement with the shifts found for covalency increase. Therefore, a plausible explanation is that geometry changes in  $Ni_x(Fe_{1-x})O_yH_z$  toward noncentrosymmetric structures for more oxidizing potentials above 1.48  $V_{RHE}$  causes an enhanced p-d mixing between ligand and metal.

The absence of inversion symmetry in square pyramidal coordination enhances orbital mixing. From the character table for the  $C_{4\nu}$  point group, we note that Fe p and some d orbitals have A<sub>1</sub> and E symmetry, as do some orbitals formed by O/ OH ligand p orbitals. This means a stronger p-d mixing between ligand metal orbitals at a potential of 1.48 V<sub>RHE</sub> compared to distorted Oh symmetry in the resting state (see Analysis of the adsorption pre-edge by HERFD for more detailed information). Thus, a change in the local surrounding environment (coordination number; geometric transformations from  $O_h$  to  $C_{4\nu}$ ) of Fe during OER leads to spectral modification through the altered degree of covalency of the metal-ligand (Fe-O) bond. This spectral response to coordination environment changes is observed not only in EXAFS as well as in experimental and theoretical HERFD but also in the  $K\beta$  spectra (Figure 5B) in favor of the interpretation of  $C_{4v}$  symmetry around Fe(III) in the active OER catalyst. Another argument suggesting that the  $C_{4\nu}$  coordination has a more covalent character than that of Oh is the shorter bond distance in the former<sup>44</sup> (see, also, EXAFS data above). In the ligand field depiction of  $C_{4\nu}$  compared to  $O_h$  coordination, the high spin Fe(III) center has more unpaired electrons in the d orbitals of e and a1 symmetries. Orbitals of these symmetries tend to form ligand bonds with more covalent character than the other orbitals that transform to b2 and b1 symmetries, as found in  $O_{\rm h}$  coordination. Similar  $K\beta$  spectra evolution for different local coordination environments was reported by Lafueza et al.<sup>44</sup> for Fe(III) and by Peng et al.<sup>74</sup> for Mn(II), which is an isoelectronic  $(3d^5)$  configuration to Fe(III) compounds. The situation is reversed for the  $O_h$  coordination case (see Analysis of the adsorption pre-edge by HERFD XAS for more details).

The conclusions drawn from the  $K\beta$  analysis align with the Fe  $K\alpha$  results. Specifically, the absence of significant changes in the  $K\alpha$  spectra between the active and resting states of the electrocatalyst material (Figure 5A) is consistent with previously reported effects of geometric changes in high-spin Fe(III) complexes. These findings suggest that the observed spectral differences are attributable to structural rearrangements rather than changes in spin or oxidation state, as further elaborated in the Supporting Information.

**Energetics from DFT Calculations.** In order to shed further light on the most likely state of Fe under resting and operational conditions, DFT calculations were carried out comparing the energetics of different Fe-doped model structures. Models evaluating energetic trends include dilute (~6%) Fe in nonintercalating α-NiO<sub>2</sub>, β-NiOOH, and β-Ni(OH)<sub>2</sub> as well as fully H<sub>2</sub>O and ion (K<sup>+</sup> or NO<sub>3</sub><sup>-</sup>) intercalated α-Ni(OH)<sub>2</sub> and γ-NiOOH type structures with 10% Fe.<sup>32,97</sup> We also studied increased Fe-doping (25%) for the nonintercalating structures. The higher concentrations of Fe better represent the average expected Fe concentration from the experimental synthesis protocol. However, such higher concentrations do not allow for full control over the effects on the Fe center from varying the NiO<sub>2</sub>H<sub>z</sub> scaffolding environment as any change in the Fe structure or oxidation

simultaneously affects the  $\mathrm{NiO}_y\mathrm{H}_z$  scaffold. Thus, we use the low Fe-concentration models to gain valuable insights into the influence of the scaffold under a constant Fe oxidation state (as modeled by the number of O/OH ligands). In addition, although fully intercalated structures are expected from the experiments, there are large degrees of freedom in these structures. The ion-impregnated intercalating aqueous layer can be arranged in multiple ways. This warrants a complementary systematic study of more well-defined non-intercalating structures as a comparison to the calculations with intercalating models. We also evaluate the formation of  $\mathrm{Ni}_x(\mathrm{Fe}_{1-x})\mathrm{O}_y\mathrm{H}_z$  with Fe in a  $C_{4\nu}$  compared to  $O_\mathrm{h}$  coordination environment for the active catalyst under OER potentials.

The high-spin state was always found to be the most favorable for Fe in  $Ni_x(Fe_{1-x})O_yH_z$ . For Ni, the Ni(+2.00) structure is in a triplet states, whereas Ni(+3.00) and Ni(+4.00) are low spins. (Note that we use numerical values in this section to allow for noninteger, average, oxidation states.) In the general case, both Fe and Ni prefer a ferromagnetic (FM) internal spin arrangement in the  $Ni_x(Fe_{1-x})O_vH_z$ , structures (note that this is not always the case for pure Ni samples) with the Fe and Ni in a mutual antiferromagnetic (AFM) arrangement. This ordering was also found for the NiO2 scaffolds, although the Ni magnetic moments are close to zero. For the nonintercalating structures and for  $\alpha$ -Ni(OH)<sub>2</sub>, local magnetic moments and computed Bader charges for the compounds followed the expected values corresponding to a given Ni or Fe formal oxidation state as reported by Zhao et al. 99 γ-NiOOH was the exception where Fe in the formal Fe(+3.33) and Fe(+3.67) positions both give magnetic moments (4.25). Bader charges (+1.71) that best corresponds to Fe(+3.00). This indicates that Ni prefers to carry the excess charge beyond +3.00 so that Ni is oxidized while Fe remains Fe(+3.00).

Figure 6 compares the energetics at varied potential biases for different  $Ni_r(Fe_{1-r})O_rH_z$  structures with Fe in  $O_h$ symmetry. Starting from the 25% Fe-doped nonintercalating model structures, Figure 6 (left) shows the relative free energy per metal atom ( $\Delta G = \Delta G/n$ , with n being the number of metal atoms in the model) of Fe at +2.00 to +4.00 oxidation state in different nonintercalated NiO<sub>v</sub>H<sub>z</sub> scaffolds as a function of potential. Energies are given relative to Fe(+3.00). At  $U = 1.10 \text{ V}_{\text{RHE}}$ , Fe(+3.00) is favored for all scaffold structures except in the  $NiO_2$  in which Fe(+2.67) is preferred. As the potential is increased, more oxidized states of Fe become favored. For the Ni(OH)<sub>2</sub> scaffold, this happens early at 1.2 V<sub>RHE</sub>, for NiOOH at 1.65 V<sub>RHE</sub>, and for the NiO<sub>2</sub> scaffold at 1.5 V<sub>RHE</sub>. Hence, at low potential corresponding to the catalyst resting state, a Fe(+3.00) state is predicted, whereas the transition from Fe(3.00) to Fe(4.00) could occur before or just after the 1.66  $V_{\text{RHE}}$ . We note that the transition could be kinetically limited and that an applied overpotential exceeding the predicted reversible potentials might be needed to spark the oxidation, explaining the lack of the inferred oxidation state experimentally. Figure S15 compares the energetics of all oxidation states in all nonintercalated NiO<sub>v</sub>H<sub>z</sub> scaffolds. This indicates that  $Ni(OH)_2$  and  $NiO_2$  are favored at the 1.10  $V_{\text{RHE}}$  and 1.66  $V_{\text{RHE}}$  potentials, respectively, with Fe likely in a Fe(+3.00) state.

Comparing the above results to the low Fe-doping case gives a similar picture with few exceptions. As above, in the  $Ni(OH)_2$  scaffold and at 1.10  $V_{RHE}$ , Fe prefers a Fe(+3.00) oxidation state, but at the higher potential, it becomes

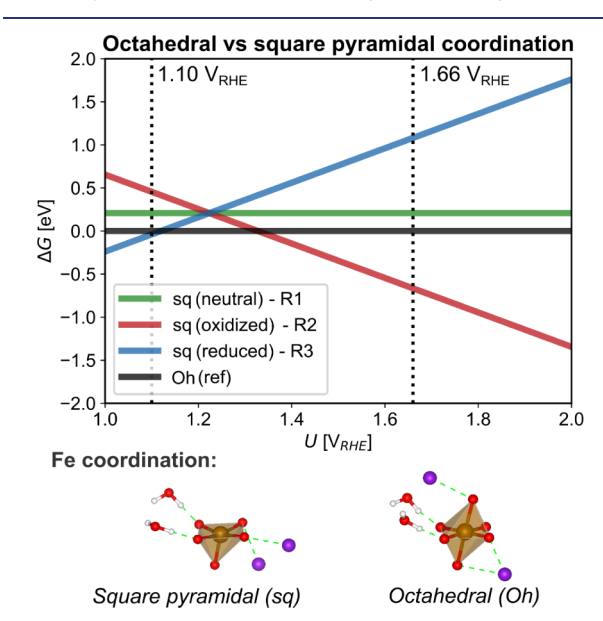
Fe(+4.00). In the NiO<sub>2</sub> scaffold, an oxidation state between Fe(+3.67) to Fe(+3.00) is favored, but Fe(+4.00) is preferred at the 1.66  $V_{RHE}$  potential. In contrast to the above, for the NiOOH scaffold, the Fe(+3.00) is preferred throughout, which is best explained by the large penalty of breaking the H-bonding network to create Ni(Fe)O<sub>2</sub>.

In addition, we need to account for the effect of intercalation between the  $Ni_x(Fe_{1-x})O_yH_z$  layers. As stated before, intercalated structures are expected experimentally, and the lack of direct interactions between the  $Ni_x(Fe_{1-x})O_vH_z$  layers could influence the relative energetics of different oxidation states significantly. For  $\alpha$ -Ni(OH)<sub>2</sub>, we create a NO<sub>3</sub><sup>-</sup> intercalated structure based on the experimental conditions and previously optimized structures of Dionigi et al.<sup>32</sup> Fe doping was accounted for with Fe evaluated in all unique Ni positions. While the energy difference for Fe(+2.00) was moderate between the different positions ( $\pm 0.1$  eV), the most favorable positions for creating Fe (+3.00) are shown in Figure 6; creating Fe(+3.00) is favorable relative to other oxidation states (and positions) if Fe is placed in an initial environment where two OH ligands lack H-bonds to intercalating water. Shifting these OH into O (plus another previously H-bonded OH, yielding three O in total) to create Fe(+3.00) is favorable at low potentials (1.10  $V_{RHE}$ ), but not at higher potentials, which is in line with our results from the nonintercalating models. For  $\gamma$ -NiOOH, the intercalating layer contains K<sup>+</sup> and water.  $^{29,97}$  As no H are part of the structure, the amount of  $\mathrm{K}^{+}$ sets the formal oxidation state to Fe (+3.67) and Ni(+3.67) on average. From these structures, as shown in Figure 6 for the lowest energy cases, adding additional H around Fe to create a formal Fe(+3.00), is not beneficial. This is likely influenced by the disrupted H-bonding network upon addition of extra H. Nevertheless, an alternative interpretation is that Fe is already Fe(+3.00) in the  $\gamma$ -NiOOH state, and that Ni centers carry the excess charge left from Fe; hence Ni is approximately Ni(+4.00) while Fe is Fe(+3.00). This interpretation is also supported by the computed local magnetic moment and Bader charge of the Fe (see above) that favors a Fe(+3.00) oxidation state based on a comparison to previous reports.<sup>99</sup>

For the case of O<sub>h</sub> coordination environments evaluated above we can draw a few conclusions; whereas the DFT energetics results do not fully resolve the character of Fe in Fedoped NiO<sub>v</sub>H<sub>z</sub>, they do favor a picture where Fe(+3.00) oxidation state is preferred at the lower applied potentials ( $\sim$ 1.10 V<sub>RHE</sub>) and that the stability region of Fe(+3.00) likely stretches up to 1.66  $V_{\text{RHE}}$ . The latter finding is also feasible for the γ-NiOOH fully intercalated structure that, based on previous experimental findings, is expected to be the prevailing structure at 1.66 V<sub>RHE</sub>. Therefore, together with the reasonable agreement between experimental and simulated XANES pre-edge and EXAFS data, a plausible interpretation is that the character of Fe is predominantly Fe(+3.00) in an  $O_b$ environment at OER operation conditions. In this picture, the spectral changes in XAS and XES data compared to the resting state can be explained by a variation in the local coordination environment that is a direct consequence of varying O/OH bonds in the NiO<sub>v</sub>H<sub>z</sub> scaffold. While the above conclusion cannot be rejected, the combined support for Fe(+3.00) in a square pyramidal 5-fold coordination  $(C_{4\nu})$  as the active state in OER catalysis is deemed stronger, as further explained below.

Lastly, we address the possibility of generating an active Fe state in a  $C_{4\nu}$  symmetry and compare it to the picture above in

which Fe remains Fe(+3.00) in an  $O_h$  coordination environment. Figure 7 shows the free energy of forming a local FeO<sub>5</sub>



Octahedral to square pyramidal transitions (γ-NiOOH):

**R1**: Ni<sub>5</sub>FeO<sub>12</sub>K<sub>2</sub>  $\rightarrow$  Ni<sub>5</sub>FeO<sub>11</sub>K<sub>2</sub> +  $\frac{1}{2}$ O<sub>2</sub>(g)

**R2**:  $Ni_5FeO_{12}K_2 + H_2O(I) \rightarrow Ni_5FeO_{11}K_2 + O_2(g) + 2(H^++e^-)$ 

**R3**: Ni<sub>5</sub>FeO<sub>12</sub>K<sub>2</sub> + 2(H<sup>+</sup>+e<sup>-</sup>)  $\rightarrow$  Ni<sub>5</sub>FeO<sub>11</sub>K<sub>2</sub> + H<sub>2</sub>O(I)

**Figure 7.** DFT results for Fe-doped γ-NiOOH with Fe as Fe(III) in  $C_{4v}$  coordination. Energetics comparing  $O_h$  to  $C_{4v}$  coordination around Fe through reaction R1–3 at various resting to OER active potentials.

structure from FeO<sub>6</sub> in  $\gamma$ -NiOOH by either a neutral/chemical (R1), oxidative (R2), or reductive (R3) reaction. In our model, Fe-doped γ-NiOOH is simulated by the water and K<sup>+</sup> intercalated Ni<sub>5</sub>FeO<sub>12</sub>K<sub>2</sub> structure (same as in Figure 6.) that evolves into Ni<sub>5</sub>FeO<sub>11</sub>K<sub>2</sub> through the simultaneous formation of  $O_2$  or  $H_2O$  (see R1-3 in Figure 7). We find that the distorted O<sub>h</sub> reference structure is preferred at potentials below ~1.25  $V_{RHE}$ , whereas oxidative formation of the  $C_{4\nu}$  is preferred at higher potentials corresponding to the potentials probed during OER evolution. Square pyramidal intermediate states are indeed part of the majority of the proposed catalytic mechanisms of  $O_2(g)$  formation using  $Ni_x(Fe_{1-x})O_yH_z$  electrocatalysts.  $^{100,101}$  As  $O_2$  evolution is ongoing at these potentials, it is thus reasonable to assume the  $C_{4\nu}$  structure in Figure 7 is kinetically accessible. Figure 4C also demonstrates that the simulated XANES pre-edge spectra is compatible with the experimental results; the pre-edge consists of a single component and its intensity is significantly increased compared to the resting. In addition, the EXAFS spectra simulated for the  $C_{4\nu}$  state are also in good agreement with experimental data (Figure 4A). Hence, we conclude that Fe(+3.00) in a  $C_{4\nu}$ coordination-possibly in dynamic equilibrium with O<sub>h</sub> Fe(+3.00) – is a likely active state for the  $Ni_x(Fe_{1-x})O_vH_z$ catalysts material at OER potentials.

## CONCLUSION

In this work, we have employed a host of X-ray spectroscopy techniques, including HERFD XANES, EXAFS, as well as  $K\alpha$  and  $K\beta$  XES, to examine the electronic and local structural

evolution of the Fe site in  $Ni_x(Fe_{1-x})O_yH_z$  electrocatalyst in situ at different electrochemical potentials. These range from a resting state (1.10 V<sub>RHE</sub>) to oxidized and catalytically active  $(1.66 V_{RHE})$  states of the electrocatalyst. Our results give a detailed picture of the equilibrium state of the catalysts under the applied conditions. At the resting state, the Fe-doped  $NO_3^-(aq)$  intercalated  $\alpha$ -Ni(OH)<sub>2</sub> phase matched best the combined experimental and DFT results, while under catalytic conditions, the best match is represented by Fe-doped  $\gamma$ -NiOOH with intercalated and solvated  $K^+(aq)$  ions. Moreover, through experimental observation and comparison to DFT electronic structure simulations, we are able to assign variations in spectral features to different Fe local coordination environments that correspond to changes in the degree of pd mixing between O/OH ligand 2p states and the 3d and 4p states of Fe. More specifically, we find that the chemical picture of the  $Ni_x(Fe_{1-x})O_vH_z$  catalysts that best fits the observed results is a FeO<sub>v</sub>H<sub>z</sub> center that exhibits substantial distortions from the  $O_{\rm b}$  geometry (found at the resting state potential) with Fe remaining at all potentials at a formal Fe(III) oxidation state within the studied 1.10-1.66 V<sub>RHE</sub> potential range. Spectral changes are associated with alterations in the covalency of the Fe-O bonds. These changes are induced by O ligand dissociation leading to a local geometry change from distorted  $O_h$  to  $C_{4v}$  and a simultaneous oxidation of the NiO, H, scaffold caused by the applied potential bias. This surprising result allow us to speculate that the Fe active site under OER operation has a weakly coordinated or easily dissociable ligand. The active site would then have the flexibility to be five- or six-coordinate, depending on the applied potential, consistent with its catalytic function. An easily dissociable ligand would provide the required substrate oxygen for O-O bond formation and readily available sites during the catalytic cycle to bind intermediate species.

### ASSOCIATED CONTENT

## Supporting Information

The Supporting Information is available free of charge at https://pubs.acs.org/doi/10.1021/jacs.4c13417.

Additional figures and a table that provide further details on sample preparation, experimental and computational methodologies, EXAFS simulations performed using FEFF, atomic model scaffold structures considered in this study, linear regression fitting of theoretical compounds, simulated XAS for Fe in diverse environments, XES data analysis procedures, computed energetics of Fe in various oxidation states and  $\mathrm{NiO_yH_z}$  scaffolds, and sample characterization information (PDF)

## AUTHOR INFORMATION

### **Corresponding Author**

Sergey Koroidov — Department of Physics, Alba Nova Research Center, Stockholm University, Stockholm SE-106 91, Sweden; Wallenberg Initiative Materials Science for Sustainability (WISE), Department of Physics, Stockholm University, Stockholm SE-106 91, Sweden; orcid.org/ 0000-0003-4823-2188; Email: sergey.koroidov@ fysik.su.se

#### **Authors**

Joakim Halldin Stenlid — Department of Physics, Alba Nova Research Center, Stockholm University, Stockholm SE-106 91, Sweden; SUNCAT Center for Interface Science and Catalysis, SLAC National Accelerator Laboratory, Menlo Park, California 94025, United States; SUNCAT Center for Interface Science and Catalysis, Department of Engineering, Stanford University, Stanford, California 94305, United States; orcid.org/0000-0003-3832-2331

Mikaela Görlin — Department of Physics, Alba Nova Research Center, Stockholm University, Stockholm SE-106 91, Sweden; Department of Chemistry, Ångström Laboratory, Uppsala University, Uppsala SE-751 21, Sweden; orcid.org/0000-0003-4472-955X

Oscar Diaz-Morales – Department of Physics, Alba Nova Research Center, Stockholm University, Stockholm SE-106 91, Sweden; Holst Centre, Netherlands Organisation for Applied Scientific Research, Eindhoven 5656, the Netherlands; orcid.org/0000-0003-1221-0809

Bernadette Davies — Department of Physics, Alba Nova Research Center, Stockholm University, Stockholm SE-106 91, Sweden; Orcid.org/0000-0001-7122-2231

Vladimir Grigorev — Department of Physics, Alba Nova Research Center, Stockholm University, Stockholm SE-106 91, Sweden; Wallenberg Initiative Materials Science for Sustainability (WISE), Department of Physics, Stockholm University, Stockholm SE-106 91, Sweden

David Degerman — Department of Physics, Alba Nova Research Center, Stockholm University, Stockholm SE-106 91, Sweden; Wallenberg Initiative Materials Science for Sustainability (WISE), Department of Physics, Stockholm University, Stockholm SE-106 91, Sweden; ○ orcid.org/ 0000-0001-6085-2916

Aleksandr Kalinko – Department of Chemistry and Center for Sustainable Systems Design (CSSD), University of Paderborn, Paderborn D-33098, Germany; Deutsches Elektronen-Synchrotron DESY, Hamburg D-22607, Germany

Mia Börner — Department of Physics, Alba Nova Research Center, Stockholm University, Stockholm SE-106 91, Sweden Mikhail Shipilin — Department of Physics, Alba Nova Research Center, Stockholm University, Stockholm SE-106 91, Sweden

Matthias Bauer – Department of Chemistry and Center for Sustainable Systems Design (CSSD), University of Paderborn, Paderborn D-33098, Germany; ⊚ orcid.org/0000-0002-9294-6076

Alessandro Gallo – SUNCAT Center for Interface Science and Catalysis, SLAC National Accelerator Laboratory, Menlo Park, California 94025, United States; SUNCAT Center for Interface Science and Catalysis, Department of Engineering, Stanford University, Stanford, California 94305, United States; Sila Nanotechnologies, Alameda, California 94501, United States

Frank Abild-Pedersen — SUNCAT Center for Interface Science and Catalysis, SLAC National Accelerator Laboratory, Menlo Park, California 94025, United States; orcid.org/0000-0002-1911-074X

Michal Bajdich – SUNCAT Center for Interface Science and Catalysis, SLAC National Accelerator Laboratory, Menlo Park, California 94025, United States

Anders Nilsson — Department of Physics, Alba Nova Research Center, Stockholm University, Stockholm SE-106 91, Sweden; SUNCAT Center for Interface Science and Catalysis, SLAC National Accelerator Laboratory, Menlo Park, California 94025, United States; Wallenberg Initiative Materials Science for Sustainability (WISE), Department of Physics, Stockholm University, Stockholm SE-106 91, Sweden; orcid.org/0000-0003-1968-8696

Complete contact information is available at: https://pubs.acs.org/10.1021/jacs.4c13417

#### **Author Contributions**

<sup>11</sup>J.H.S. and M.G. contributed equally.

#### Notes

The authors declare no competing financial interest.

### ACKNOWLEDGMENTS

We gratefully acknowledge funding from the Knut and Alice Wallenberg Foundation, WISE, the Swedish Research Council and the Swedish strategic research program StandUp for Energy. This research was supported in part by the U.S. Department of Energy, Office of Science, Office of Basic Energy Sciences, Chemical Sciences, Geosciences, and Biosciences Division, Catalysis Science Program to the SUNCAT Center for Interface Science and Catalysis. J.H.S. gratefully acknowledge a postdoc fellowship from the Knut and Alice Wallenberg Foundation (Grant No. 2019.0586). M.G. acknowledges financial support from the ÅForsk Foundation (grant no. 21-384), the Sweden-America foundation, the Blanceflor Boncompagni-Ludovisi foundation, and Royal Swedish Academy of Engineering Sciences. We acknowledge computational support from the National Energy Research Scientific Computing Center (Project Allocation No. m2997), a Department of Energy Office of Science User Facility supported by the Office of Science of the U.S. Department of Energy under Contract No. DE-AC02-05CH11231.

# REFERENCES

- (1) Lewis, N. S.; Nocera, D. G. Powering the Planet: Chemical Challenges in Solar Energy Utilization. *Proc. Natl. Acad. Sci. U. S. A.* **2006**, 103 (43), 15729–15735.
- (2) Park, S.; Shao, Y.; Liu, J.; Wang, Y. Oxygen Electrocatalysts for Water Electrolyzers and Reversible Fuel Cells: Status and Perspective. *Energy Environ. Sci.* **2012**, *5* (11), 9331–9344.
- (3) Stamenkovic, V. R.; Strmcnik, D.; Lopes, P. P.; Markovic, N. M. Energy and Fuels from Electrochemical Interfaces. *Nat. Mater.* **2017**, *16* (1), 57–69.
- (4) Młynarek, G.; Paszkiewicz, M.; Radniecka, A. The Effect of Ferric Ions on the Behaviour of a Nickelous Hydroxide Electrode. *J. Appl. Electrochem.* **1984**, *14* (2), 145–149.
- (\$) Trotochaud, L.; Ranney, J. K.; Williams, K. N.; Boettcher, S. W. Solution-Cast Metal Oxide Thin Film Electrocatalysts for Oxygen Evolution. *J. Am. Chem. Soc.* **2012**, *134* (41), 17253–17261.
- (6) Gong, M.; Li, Y.; Wang, H.; Liang, Y.; Wu, J. Z.; Zhou, J.; Wang, J.; Regier, T.; Wei, F.; Dai, H. An Advanced Ni–Fe Layered Double Hydroxide Electrocatalyst for Water Oxidation. *J. Am. Chem. Soc.* 2013, 135 (23), 8452–8455.
- (7) Klaus, S.; Cai, Y.; Louie, M. W.; Trotochaud, L.; Bell, A. T. Effects of Fe Electrolyte Impurities on Ni(OH)<sub>2</sub>/NiOOH Structure and Oxygen Evolution Activity. *J. Phys. Chem. C* **2015**, *119* (13), 7243–7254.
- (8) Louie, M. W.; Bell, A. T. An Investigation of Thin-Film Ni—Fe Oxide Catalysts for the Electrochemical Evolution of Oxygen. *J. Am. Chem. Soc.* **2013**, *135* (33), 12329–12337.
- (9) Dionigi, F.; Strasser, P. NiFe-Based (Oxy)Hydroxide Catalysts for Oxygen Evolution Reaction in Non-Acidic Electrolytes. *Adv. Energy Mater.* **2016**, *6* (23), 1600621.

- (10) Hall, D. S.; Lockwood, D. J.; Bock, C.; MacDougall, B. R. Nickel Hydroxides and Related Materials: A Review of Their Structures, Synthesis and Properties. *Proc. R. Soc. A* **2015**, *471* (2174), 20140792.
- (11) Mahdi Najafpour, M.; Jameei Moghaddam, N. Iron Oxide Deposited on Metallic Nickel for Water Oxidation. *Sustainable Energy Fuels* **2017**, *1* (3), 658–663.
- (12) Madadkhani, S.; Aghakhanpour, R. B.; Singh, J. P.; Bagheri, R.; Chae, K. H.; Song, Z.; Najafpour, M. M. A Trimetallic Organometallic Precursor for Efficient Water Oxidation. *Sci. Rep.* **2019**, *9* (1), 3734.
- (13) Safdari, T.; Akbari, N.; Valizadeh, A.; Bagheri, R.; Song, Z.; Allakhverdiev, S. I.; Najafpour, M. M. Iron–Nickel Oxide: A Promising Strategy for Water Oxidation. *New J. Chem.* **2020**, 44 (4), 1517–1523.
- (14) Li, Y.-F.; Selloni, A. Mechanism and Activity of Water Oxidation on Selected Surfaces of Pure and Fe-Doped NiOx. ACS Catal. 2014, 4 (4), 1148–1153.
- (15) Klaus, S.; Louie, M. W.; Trotochaud, L.; Bell, A. T. Role of Catalyst Preparation on the Electrocatalytic Activity of Ni<sub>1-x</sub>Fe<sub>x</sub>OOH for the Oxygen Evolution Reaction. *J. Phys. Chem. C* **2015**, *119* (32), 18303–18316.
- (16) Song, F.; Busch, M. M.; Lassalle-Kaiser, B.; Hsu, C.-S.; Petkucheva, E.; Bensimon, M.; Chen, H. M.; Corminboeuf, C.; Hu, X. An Unconventional Iron Nickel Catalyst for the Oxygen Evolution Reaction. *ACS Cent. Sci.* **2019**, *5* (3), 558–568.
- (17) Trotochaud, L.; Young, S. L.; Ranney, J. K.; Boettcher, S. W. Nickel–Iron Oxyhydroxide Oxygen-Evolution Electrocatalysts: The Role of Intentional and Incidental Iron Incorporation. *J. Am. Chem. Soc.* **2014**, *136* (18), *6744*–*6753*.
- (18) Friebel, D.; Louie, M. W.; Bajdich, M.; Sanwald, K. E.; Cai, Y.; Wise, A. M.; Cheng, M.-J.; Sokaras, D.; Weng, T.-C.; Alonso-Mori, R.; Davis, R. C.; Bargar, J. R.; Nørskov, J. K.; Nilsson, A.; Bell, A. T. Identification of Highly Active Fe Sites in (Ni,Fe)OOH for Electrocatalytic Water Splitting. *J. Am. Chem. Soc.* **2015**, *137* (3), 1305–1313.
- (19) Chung, D. Y.; Lopes, P. P.; Farinazzo Bergamo Dias Martins, P.; He, H.; Kawaguchi, T.; Zapol, P.; You, H.; Tripkovic, D.; Strmcnik, D.; Zhu, Y.; Seifert, S.; Lee, S.; Stamenkovic, V. R.; Markovic, N. M. Dynamic Stability of Active Sites in Hydr(Oxy)-Oxides for the Oxygen Evolution Reaction. *Nat. Energy* **2020**, *5* (3), 222–230.
- (20) Li, N.; Bediako, D. K.; Hadt, R. G.; Hayes, D.; Kempa, T. J.; von Cube, F.; Bell, D. C.; Chen, L. X.; Nocera, D. G. Influence of Iron Doping on Tetravalent Nickel Content in Catalytic Oxygen Evolving Films. *Proc. Natl. Acad. Sci. U. S. A.* **2017**, *114* (7), 1486–1491.
- (21) Yang, L.; Liu, Z.; Zhu, S.; Feng, L.; Xing, W. Ni-Based Layered Double Hydroxide Catalysts for Oxygen Evolution Reaction. *Mater. Today Phys.* **2021**, *16*, 100292.
- (22) Vandichel, M.; Laasonen, K.; Kondov, I. Oxygen Evolution and Reduction on Fe-Doped NiOOH: Influence of Solvent, Dopant Position and Reaction Mechanism. *Top. Catal.* **2020**, *63* (9), 833–845
- (23) Vandichel, M.; Busch, M.; Laasonen, K. Oxygen Evolution on Metal-Oxy-Hydroxides: Beneficial Role of Mixing Fe, Co, Ni Explained via Bifunctional Edge/Acceptor Route. *ChemCatChem* **2020**, *12* (5), 1436–1442.
- (24) Xiao, H.; Shin, H.; Goddard, W. A. Synergy between Fe and Ni in the Optimal Performance of (Ni,Fe)OOH Catalysts for the Oxygen Evolution Reaction. *Proc. Natl. Acad. Sci. U. S. A.* **2018**, *115* (23), 5872–5877.
- (25) Jin, Y.; Huang, S.; Yue, X.; Du, H.; Shen, P. K. Mo- and Fe-Modified Ni(OH)<sub>2</sub>/NiOOH Nanosheets as Highly Active and Stable Electrocatalysts for Oxygen Evolution Reaction. *ACS Catal.* **2018**, *8* (3), 2359–2363
- (26) Costanzo, F. Effect of Doping  $\beta$ -NiOOH with Co on the Catalytic Oxidation of Water: DFT+U Calculations. *Phys. Chem. Phys.* **2016**, *18* (10), 7490–7501.

- (27) Li, Y.-F.; Li, J.-L.; Liu, Z.-P. Structure and Catalysis of NiOOH: Recent Advances on Atomic Simulation. *J. Phys. Chem. C* **2021**, 125 (49), 27033–27045.
- (28) Tripkovic, V.; Hansen, H. A.; Vegge, T. From 3D to 2D Co and Ni Oxyhydroxide Catalysts: Elucidation of the Active Site and Influence of Doping on the Oxygen Evolution Activity. *ACS Catal.* **2017**, *7* (12), 8558–8571.
- (29) Görlin, M.; Halldin Stenlid, J.; Koroidov, S.; Wang, H.-Y.; Börner, M.; Shipilin, M.; Kalinko, A.; Murzin, V.; Safonova, O. V.; Nachtegaal, M.; Uheida, A.; Dutta, J.; Bauer, M.; Nilsson, A.; Diaz-Morales, O. Key Activity Descriptors of Nickel-Iron Oxygen Evolution Electrocatalysts in the Presence of Alkali Metal Cations. *Nat. Commun.* 2020, 11 (1), 6181.
- (30) Chen, J. Y. C.; Dang, L.; Liang, H.; Bi, W.; Gerken, J. B.; Jin, S.; Alp, E. E.; Stahl, S. S. Operando Analysis of NiFe and Fe Oxyhydroxide Electrocatalysts for Water Oxidation: Detection of Fe4+ by Mössbauer Spectroscopy. *J. Am. Chem. Soc.* **2015**, *137* (48), 15090–15093.
- (31) Hunter, B. M.; Thompson, N. B.; Müller, A. M.; Rossman, G. R.; Hill, M. G.; Winkler, J. R.; Gray, H. B. Trapping an Iron(VI) Water-Splitting Intermediate in Nonaqueous Media. *Joule* **2018**, 2 (4), 747–763.
- (32) Dionigi, F.; Zeng, Z.; Sinev, I.; Merzdorf, T.; Deshpande, S.; Lopez, M. B.; Kunze, S.; Zegkinoglou, I.; Sarodnik, H.; Fan, D.; Bergmann, A.; Drnec, J.; de Araujo, J. F.; Gliech, M.; Teschner, D.; Zhu, J.; Li, W.-X.; Greeley, J.; Cuenya, B. R.; Strasser, P. In-Situ Structure and Catalytic Mechanism of NiFe and CoFe Layered Double Hydroxides during Oxygen Evolution. *Nat. Commun.* 2020, 11 (1), 2522.
- (33) de Groot, F.; Kotani, A. Core Level Spectroscopy of Solids; CRC Press, 2008.
- (34) de Groot, F. High-Resolution X-Ray Emission and X-Ray Absorption Spectroscopy. *Chem. Rev.* **2001**, *101* (6), 1779–1808.
- (35) Koroidov, S.; Winiwarter, A.; Diaz-Morales, O.; Görlin, M.; Stenlid, J. H.; Wang, H.-Y.; Börner, M.; Goodwin, C. M.; Soldemo, M.; Pettersson, L. G. M.; et al. Chemisorbed Oxygen or Surface Oxides Steer the Selectivity in Pd Electrocatalytic Propene Oxidation Observed by Operando Pd L-Edge X-Ray Absorption Spectroscopy. *Catal. Sci. Technol.* **2021**, *11* (10), 3347–3352.
- (36) Juhin, A.; de Groot, F.; Vankó, G.; Calandra, M.; Brouder, C. Angular Dependence of Core Hole Screening in LiCoO<sub>2</sub>: A DFT+U Calculation of the Oxygen and Cobalt \$K\$-Edge x-Ray Absorption Spectra. *Phys. Rev. B* **2010**, *81* (11), 115115.
- (37) Friebel, D.; Bajdich, M.; Yeo, B. S.; Louie, M. W.; Miller, D. J.; Casalongue, H. S.; Mbuga, F.; Weng, T.-C.; Nordlund, D.; Sokaras, D.; et al. On the Chemical State of Co Oxide Electrocatalysts during Alkaline Water Splitting. *Phys. Chem. Chem. Phys.* **2013**, *15* (40), 17460–17467.
- (38) Tesch, M. F.; Bonke, S. A.; Jones, T. E.; Shaker, M. N.; Xiao, J.; Skorupska, K.; Mom, R.; Melder, J.; Kurz, P.; Knop-Gericke, A.; Schlögl, R.; Hocking, R. K.; Simonov, A. N. Evolution of Oxygen—Metal Electron Transfer and Metal Electronic States During Manganese Oxide Catalyzed Water Oxidation Revealed with In Situ Soft X-Ray Spectroscopy. *Angew. Chem., Int. Ed.* **2019**, 58 (11), 3426—3432.
- (39) Nong, H. N.; Falling, L. J.; Bergmann, A.; Klingenhof, M.; Tran, H. P.; Spöri, C.; Mom, R.; Timoshenko, J.; Zichittella, G.; Knop-Gericke, A.; Piccinin, S.; Pérez-Ramírez, J.; Cuenya, B. R.; Schlögl, R.; Strasser, P.; Teschner, D.; Jones, T. E. Key Role of Chemistry versus Bias in Electrocatalytic Oxygen Evolution. *Nature* **2020**, *587* (7834), 408–413.
- (40) Chakthranont, P.; Kibsgaard, J.; Gallo, A.; Park, J.; Mitani, M.; Sokaras, D.; Kroll, T.; Sinclair, R.; Mogensen, M. B.; Jaramillo, T. F. Effects of Gold Substrates on the Intrinsic and Extrinsic Activity of High-Loading Nickel-Based Oxyhydroxide Oxygen Evolution Catalysts. ACS Catal. 2017, 7 (8), 5399–5409.
- (41) Görlin, M.; Chernev, P.; Ferreira de Araújo, J.; Reier, T.; Dresp, S.; Paul, B.; Krähnert, R.; Dau, H.; Strasser, P. Oxygen Evolution Reaction Dynamics, Faradaic Charge Efficiency, and the Active Metal

- Redox States of Ni-Fe Oxide Water Splitting Electrocatalysts. J. Am. Chem. Soc. 2016, 138 (17), 5603-5614.
- (42) Smith, R. D. L.; Pasquini, C.; Loos, S.; Chernev, P.; Klingan, K.; Kubella, P.; Mohammadi, M. R.; González-Flores, D.; Dau, H. Geometric Distortions in Nickel (Oxy)Hydroxide Electrocatalysts by Redox Inactive Iron Ions. *Energy Environ. Sci.* **2018**, *11* (9), 2476–2485.
- (43) Heijboer, W. M.; Glatzel, P.; Sawant, K. R.; Lobo, R. F.; Bergmann, U.; Barrea, R. A.; Koningsberger, D. C.; Weckhuysen, B. M.; de Groot, F. M. F.  $K\beta$ -Detected XANES of Framework-Substituted FeZSM-5 Zeolites. *J. Phys. Chem. B* **2004**, *108* (28), 10002–10011.
- (44) Lafuerza, S.; Carlantuono, A.; Retegan, M.; Glatzel, P. Chemical Sensitivity of  $K\beta$  and  $K\alpha$  X-Ray Emission from a Systematic Investigation of Iron Compounds. *Inorg. Chem.* **2020**, 59 (17), 12518–12535.
- (45) Glatzel, P.; Bergmann, U. High Resolution 1s Core Hole X-Ray Spectroscopy in 3d Transition Metal Complexes—Electronic and Structural Information. *Coord. Chem. Rev.* **2005**, 249 (1), 65–95.
- (46) Pollock, C. J.; Delgado-Jaime, M. U.; Atanasov, M.; Neese, F.; DeBeer, S.  $K\beta$  Mainline X-Ray Emission Spectroscopy as an Experimental Probe of Metal–Ligand Covalency. *J. Am. Chem. Soc.* **2014**, 136 (26), 9453–9463.
- (47) Boubnov, A.; Carvalho, H. W. P.; Doronkin, D. E.; Günter, T.; Gallo, E.; Atkins, A. J.; Jacob, C. R.; Grunwaldt, J.-D. Selective Catalytic Reduction of NO Over Fe-ZSM-5: Mechanistic Insights by Operando HERFD-XANES and Valence-to-Core X-Ray Emission Spectroscopy. J. Am. Chem. Soc. 2014, 136 (37), 13006–13015.
- (48) Bair, R. A.; Goddard, W. A. Ab Initio Studies of the X-Ray Absorption Edge in Copper Complexes. I. Atomic Cu<sup>2+</sup> and Cu(Ii) Cl<sub>2</sub>. *Phys. Rev. B* **1980**, 22 (6), 2767–2776.
- (49) Brouder, C. Angular Dependence of X-Ray Absorption Spectra. *J. Phys.: Condens. Matter* **1990**, *2* (3), 701.
- (50) Westre, T. E.; Kennepohl, P.; DeWitt, J. G.; Hedman, B.; Hodgson, K. O.; Solomon, E. I. A Multiplet Analysis of Fe K-Edge 1s → 3d Pre-Edge Features of Iron Complexes. *J. Am. Chem. Soc.* **1997**, 119 (27), 6297–6314.
- (51) Chandrasekaran, P.; Stieber, S. C. E.; Collins, T. J.; Que, L., Jr.; Neese, F.; DeBeer, S. Prediction of High-Valent Iron K-Edge Absorption Spectra by Time-Dependent Density Functional Theory. *Dalton Trans.* **2011**, *40* (42), 11070–11079.
- (52) Berry, J. F.; Bill, E.; Bothe, E.; George, S. D.; Mienert, B.; Neese, F.; Wieghardt, K. An Octahedral Coordination Complex of Iron(VI). *Science* **2006**, *312* (5782), 1937–1941.
- (53) Baker, M. L.; Mara, M. W.; Yan, J. J.; Hodgson, K. O.; Hedman, B.; Solomon, E. I. K- and L-Edge X-Ray Absorption Spectroscopy (XAS) and Resonant Inelastic X-Ray Scattering (RIXS) Determination of Differential Orbital Covalency (DOC) of Transition Metal Sites. *Coord. Chem. Rev.* **2017**, 345, 182–208.
- (54) Guerlou-Demourgues, L.; Fournès, L.; Delmas, C. In Situ <sup>57</sup>Fe Mössbauer Spectroscopy Study of the Electrochemical Behavior of an Iron-Substituted Nickel Hydroxide Electrode. *J. Electrochem. Soc.* **1996**, *143* (10), 3083.
- (55) Batchellor, A. S.; Boettcher, S. W. Pulse-Electrodeposited Ni–Fe (Oxy)Hydroxide Oxygen Evolution Electrocatalysts with High Geometric and Intrinsic Activities at Large Mass Loadings. *ACS Catal.* **2015**, 5 (11), 6680–6689.
- (56) Rehr, J. J.; Kas, J. J.; Vila, F. D.; Prange, M. P.; Jorissen, K. Parameter-Free Calculations of X-Ray Spectra with FEFF9. *Phys. Chem. Chem. Phys.* **2010**, *12* (21), 5503–5513.
- (57) González-Flores, D.; Klingan, K.; Chernev, P.; Loos, S.; Mohammadi, M. R.; Pasquini, C.; Kubella, P.; Zaharieva, I.; Smith, R. D. L.; Dau, H. Nickel-Iron Catalysts for Electrochemical Water Oxidation Redox Synergism Investigated by in Situ X-Ray Spectroscopy with Millisecond Time Resolution. Sustainable Energy Fuels 2018, 2 (9), 1986–1994.
- (58) Mijovilovich, A.; Hayashi, H.; Kawamura, N.; Osawa, H.; Bruijnincx, P. C. A.; Klein Gebbink, R. J. M.; de Groot, F. M. F.; Weckhuysen, B. M. K $\beta$  Detected High-Resolution XANES of FeII and

- FeIII Models of the 2-His-1-Carboxylate Motif: Analysis of the Carboxylate Binding Mode. *Eur. J. Inorg. Chem.* **2012**, 2012 (10), 1589–1597.
- (59) Bruijnincx, P. C. A.; Lutz, M.; Spek, A. L.; Hagen, W. R.; Weckhuysen, B. M.; van Koten, G.; Gebbink, R. J. M. K. Modeling the 2-His-1-Carboxylate Facial Triad: Iron—Catecholato Complexes as Structural and Functional Models of the Extradiol Cleaving Dioxygenases. J. Am. Chem. Soc. 2007, 129 (8), 2275—2286.
- (60) Sarangi, R. X-Ray Absorption near-Edge Spectroscopy in Bioinorganic Chemistry: Application to M-O<sub>2</sub> Systems. *Coord. Chem. Rev.* **2013**, 257 (2), 459–472.
- (61) Blasco, J.; Aznar, B.; García, J.; Subías, G.; Herrero-Martín, J.; Stankiewicz, J. Charge Disproportionation in La<sub>1-x</sub>Sr<sub>x</sub>FeO<sub>3</sub> Probed by Diffraction and Spectroscopic Experiments. *Phys. Rev. B* **2008**, 77 (5), 054107.
- (62) Haaß, F.; Buhrmester, T.; Martin, M. High-Temperature in Situ X-Ray Absorption Studies on the Iron Valence in Iron-Doped Nickel Oxide ( $Ni_{1-x}Fe_x$ )<sub>1- $\delta$ </sub>O. Solid State Ionics **2001**, 141–142, 289–293.
- (63) Penner-Hahn, J. E. 2.13 X-Ray Absorption Spectroscopy. In *Comprehensive Coordination Chemistry II*, McCleverty, J. A.; Meyer, T. J., Ed.; Pergamon: Oxford, 2003, pp. 159–186. DOI: .
- (64) Cramer, S. P.; Hodgson, K. O. X-Ray Absorption Spectroscopy: A New Structural Method and Its Applications to Bioinorganic Chemistry. *Prog. Inorg. Chem.* 1979, 25, 1–39.
- (65) Gerloch, M.; Mabbs, F. E. The Crystal and Molecular Structure of NN'-Bis(Salicylideneiminato)-Iron(III)Chloride as a Five-Co-Ordinate Monomer. *J. Chem. Soc. Inorg. Phys. Theor.* **1967**, 0, 1598–1608.
- (66) Gerloch, M.; Mabbs, F. E. The Crystal and Molecular Structure of Chloro-(NN'-Bis-Salicylidene-Ethylenediamine)Iron(III) as a Hexaco-Ordinate Dimer. *J. Chem. Soc. Inorg. Phys. Theor.* **1967**, *0*, 1900–1908.
- (67) Lauffer, R. B.; Heistand, R. H. I.; Que, L., Jr. Dioxygenase Models. Crystal Structures of the 2,4-Pentanedionato, Phenanthrenesemiquinone, and Catecholato Complexes of N,N'-Ethylenebis-(Salicylideneaminato)Iron(III). *Inorg. Chem.* **1983**, 22 (1), 50–55.
- (68) Heistand, R. H. I.; Roe, A. L.; Que, L., Jr. Dioxygenase Models. Crystal Structures of [N,N'-(1,2-Phenylene)Bis(Salicylideniminato)]-(Catecholato-O)Iron(III) and.Mu.-(1,4-Benzenediolato-O,O')-Bis-[N,N'-Ethylenebis(Salicylideniminato)Iron(III)]. *Inorg. Chem.* 1982, 21 (2), 676–681.
- (69) Roe, A. L.; Schneider, D. J.; Mayer, R. J.; Pyrz, J. W.; Widom, J.; Que, L., Jr. X-Ray Absorption Spectroscopy of Iron-Tyrosinate Proteins. J. Am. Chem. Soc. 1984, 106 (6), 1676–1681.
- (70) Shulman, G. R.; Yafet, Y.; Eisenberger, P.; Blumberg, W. E. Observations and Interpretation of X-Ray Absorption Edges in Iron Compounds and Proteins. *Proc. Natl. Acad. Sci. U. S. A.* **1976**, 73 (5), 1384–1388.
- (71) Randall, C. R.; Shu, L.; Chiou, Y.-M.; Hagen, K. S.; Ito, M.; Kitajima, N.; Lachicotte, R. J.; Zang, Y.; Que, L., Jr. X-Ray Absorption Pre-Edge Studies of High-Spin Iron(II) Complexes. *Inorg. Chem.* **1995**, *34* (5), 1036–1039.
- (72) Timoshenko, J.; Roldan Cuenya, B. In Situ/Operando Electrocatalyst Characterization by X-Ray Absorption Spectroscopy. *Chem. Rev.* **2021**, *121* (2), 882–961.
- (73) Krause, M. O.; Oliver, J. H. Natural Widths of Atomic K and L Levels,  $K\alpha$  X-ray Lines and Several KLL Auger Lines. *J. Phys. Chem. Ref. Data* **1979**, 8 (2), 329–338.
- (74) Peng, G.; deGroot, F. M. F.; Haemaelaeinen, K.; Moore, J. A.; Wang, X.; Grush, M. M.; Hastings, J. B.; Siddons, D. P.; Armstrong, W. H. High-Resolution Manganese x-Ray Fluorescence Spectroscopy. Oxidation-State and Spin-State Sensitivity. *J. Am. Chem. Soc.* **1994**, *116* (7), 2914–2920.
- (75) Hämäläinen, K.; Siddons, D. P.; Hastings, J. B.; Berman, L. E. Elimination of the Inner-Shell Lifetime Broadening in x-Ray-Absorption Spectroscopy. *Phys. Rev. Lett.* **1991**, *67* (20), 2850–2853. (76) Bordiga, S.; Groppo, E.; Agostini, G.; van Bokhoven, J. A.; Lamberti, C. Reactivity of Surface Species in Heterogeneous Catalysts

- Probed by In Situ X-Ray Absorption Techniques. Chem. Rev. 2013, 113 (3), 1736–1850.
- (77) Szlachetko, J.; Nachtegaal, M.; de Boni, E.; Willimann, M.; Safonova, O.; Sa, J.; Smolentsev, G.; Szlachetko, M.; van Bokhoven, J. A.; Dousse, J.-C.; Hoszowska, J.; Kayser, Y.; Jagodzinski, P.; Bergamaschi, A.; Schmitt, B.; David, C.; Lücke, A. A von Hamos X-Ray Spectrometer Based on a Segmented-Type Diffraction Crystal for Single-Shot x-Ray Emission Spectroscopy and Time-Resolved Resonant Inelastic x-Ray Scattering Studies. *Rev. Sci. Instrum.* **2012**, 83 (10), 103105.
- (78) Glatzell, P.; Alonso-Mori, R.; Sokaras, D. Hard X-Ray Photon-in/Photon-out Spectroscopy: Instrumentation, Theory and Applications. In *X-Ray Absorption and X-Ray Emission Spectroscopy*; John Wiley & Sons, Ltd, 2016, pp. 125–153. DOI: .
- (79) Haas, O.; Vogt, U. F.; Soltmann, C.; Braun, A.; Yoon, W.-S.; Yang, X. Q.; Graule, T. The Fe K-Edge X-Ray Absorption Characteristics of  $La_{1-x}Sr_xFeO_{3-\delta}$  Prepared by Solid State Reaction. *Mater. Res. Bull.* **2009**, 44 (6), 1397–1404.
- (80) Haas, O.; Ludwig, C.; Bergmann, U.; Singh, R. N.; Braun, A.; Graule, T. X-Ray Absorption Investigation of the Valence State and Electronic Structure of  $\text{La}_{1-x}\text{Ca}_x\text{CoO}_{3-\delta}$  in Comparison with  $\text{La}_{1-x}\text{Sr}_x\text{CoO}_{3-\delta}$  and  $\text{La}_{1-x}\text{Sr}_x\text{FeO}_{3-\delta}$ . J. Solid State Chem. **2011**, 184 (12), 3163–3171.
- (81) Rohde, J.-U.; Torelli, S.; Shan, X.; Lim, M. H.; Klinker, E. J.; Kaizer, J.; Chen, K.; Nam, W.; Que, L. Structural Insights into Nonheme Alkylperoxoiron(III) and Oxoiron(IV) Intermediates by X-Ray Absorption Spectroscopy. *J. Am. Chem. Soc.* **2004**, *126* (51), 16750–16761.
- (82) Colpas, G. J.; Maroney, M. J.; Bagyinka, C.; Kumar, M.; Willis, W. S.; Suib, S. L.; Mascharak, P. K.; Baidya, N. X-Ray Spectroscopic Studies of Nickel Complexes, with Application to the Structure of Nickel Sites in Hydrogenases. *Inorg. Chem.* **1991**, *30* (5), 920–928.
- (83) Wirt, M. D.; Sagi, I.; Chen, E.; Frisbie, S. M.; Lee, R.; Chance, M. R. Geometric Conformations of Intermediates of B12 Catalysis by X-Ray Edge Spectroscopy: Cobalt(I) B12, Cobalt(II) B12, and Base-off Adenosylcobalamin. *J. Am. Chem. Soc.* **1991**, *113* (14), 5299–5304.
- (84) Leto, D. F.; Jackson, T. A. Mn K-Edge X-Ray Absorption Studies of Oxo- and Hydroxo-Manganese(IV) Complexes: Experimental and Theoretical Insights into Pre-Edge Properties. *Inorg. Chem.* **2014**, 53 (12), 6179–6194.
- (85) Neese, F. Chapter 2 Introduction to Ligand Field Theory. In *Practical Approaches to Biological Inorganic Chemistry*, Crichton, R. R.; Louro, R. O., Eds.; Elsevier: Oxford, 2013, pp. 23–51. DOI: .
- (86) Cotton, F. A. Chemical Applications of Group Theory, 2nd ed.; John Wiley & Sons Ltd.: Baffins Lane, 1972.
- (87) Figgis, B. N.; Hitchman, M. A. Ligand Field Theory and Its Applications; Wiley-VCH, John Wiley & Sons, Ltd.: New York, 2000; Vol. 14, p 354.
- (88) Vankó, G.; Neisius, T.; Molnár, G.; Renz, F.; Kárpáti, S.; Shukla, A.; de Groot, F. M. F. Probing the 3d Spin Momentum with X-Ray Emission Spectroscopy: The Case of Molecular-Spin Transitions. *J. Phys. Chem. B* **2006**, *110* (24), 11647–11653.
- (89) Svyazhin, A.; Kurmaev, E.; Shreder, E.; Shamin, S.; Sahle, C. J. Local Moments and Electronic Correlations in Fe-Based Heusler Alloys:  $K\alpha$  x-Ray Emission Spectra Measurements. *J. Alloys Compd.* **2016**, *679*, 268–276.
- (90) Kawai, J.; Suzuki, C.; Adachi, H.; Konishi, T.; Gohshi, Y. Charge-Transfer Effect on the Linewidth of Fe  $K\alpha$  x-Ray Fluorescence Spectra. *Phys. Rev. B* **1994**, *50* (16), 11347–11354.
- (91) Suzuki, C.; Kawai, J.; Tanizawa, J.; Adachi, H.; Kawasaki, S.; Takano, M.; Mukoyama, T. Local Spin Moment of LaCoO3 Probed by a Core Hole. *Chem. Phys.* **1999**, *241* (1), 17–27.
- (92) Tsutsumi, K.; Nakamori, H.; Ichikawa, K. X-Ray Mn K $\beta$  Emission Spectra of Manganese Oxides and Manganates. *Phys. Rev. B* **1976**, 13 (2), 929–933.
- (93) Castillo, R. G.; Hahn, A. W.; Van Kuiken, B. E.; Henthorn, J. T.; McGale, J.; DeBeer, S. Probing Physical Oxidation State by Resonant X-Ray Emission Spectroscopy: Applications to Iron Model

- Complexes and Nitrogenase. Angew. Chem. 2021, 133 (18), 10200–10209.
- (94) Lee, N.; Petrenko, T.; Bergmann, U.; Neese, F.; DeBeer, S. Probing Valence Orbital Composition with Iron  $K\beta$  X-Ray Emission Spectroscopy. *J. Am. Chem. Soc.* **2010**, 132 (28), 9715–9727.
- (95) Gamblin, S. D.; Urch, D. S. Metal K $\beta$  X-Ray Emission Spectra of First Row Transition Metal Compounds. *J. Electron Spectrosc. Relat. Phenom.* **2001**, *113* (2), 179–192.
- (96) Schwalenstocker, K.; Paudel, J.; Kohn, A. W.; Dong, C.; Heuvelen, K. M. V.; Farquhar, E. R.; Li, F. Cobalt  $K\beta$  Valence-to-Core X-Ray Emission Spectroscopy: A Study of Low-Spin Octahedral Cobalt(III) Complexes. *Dalton Trans.* **2016**, 45 (36), 14191–14202.
- (97) Zaffran, J.; Stevens, M. B.; Trang, C. D. M.; Nagli, M.; Shehadeh, M.; Boettcher, S. W.; Caspary Toroker, M. Influence of Electrolyte Cations on Ni(Fe)OOH Catalyzed Oxygen Evolution Reaction. *Chem. Mater.* **2017**, *29* (11), 4761–4767.
- (98) Rossiter, M. J.; Hodgson, A. E. M. A Mössbauer Study of Ferric Oxy-Hydroxide. *J. Inorg. Nucl. Chem.* **1965**, 27 (1), 63–71.
- (99) Zhao, Z.; Schlexer Lamoureux, P.; Kulkarni, A.; Bajdich, M. Trends in Oxygen Electrocatalysis of 3 D-Layered (Oxy)(Hydro)-Oxides. *ChemCatChem* **2019**, *11* (15), 3423–3431.
- (100) Feng, Z.; Dai, C.; Shi, P.; Lei, X.; Guo, R.; Wang, B.; Liu, X.; You, J. Seven Mechanisms of Oxygen Evolution Reaction Proposed Recently: A Mini Review. *Chem. Eng. J.* **2024**, *485*, 149992.
- (101) Wang, Z.; Goddard, W. A.; Xiao, H. Potential-Dependent Transition of Reaction Mechanisms for Oxygen Evolution on Layered Double Hydroxides. *Nat. Commun.* **2023**, *14* (1), 4228.